SATELLITE MEASUREMENTS OF FALLING SNOW: METHODS AND APPLICATIONS

By

George Abraham Siegel Duffy

Dissertation

Submitted to the Faculty of the

Graduate School of Vanderbilt University

in partial fulfilment of the requirements

for the degree of

DOCTOR OF PHILOSOPHY

in

Earth and Environmental Sciences

May 8, 2020

Nashville, Tennessee

Approved:

Ralf Bennartz, Ph.D

Jessica Oster, Ph.D

Jonathan Gilligan, Ph.D

Hiba Baroud, Ph.D

David Furbish, Ph.D

TABLE OF CONTENTS

PAGE

LIST OF FIGURES

LIST OF TABLES

LIST OF ABBREVIATIONS

a

MASS COEFFICIENT

APR

ADVANCED PRECIPITATION RADAR

AR

AXIAL RATIO

ArORIS

ARCTIC OBSERVATION AND REANALYSIS INTEGRATED SYSTEM

b

MASS EXPONENT

BB

BRIGHT BAND

-C

REFERRING TO A RELATIONSHIP FROM THE COMBINED DATASET

$c_{1,2}$

Z-D_M RELATIONSHIP PARAMETERS

$c_{3,4,5,6}$

DWR-D_M RELATIONSHIP PARAMETERS

DJF

DECEMBER-JANUARY-FEBRUARY

D_{liq}

LIQUID EQUIVALENT DIAMETER

D_m

MASS WEIGHTED MEAN DIAMETER

D_{max}

MAXIMUM DIAMETER OF A PARTICLE IN A PSD

D_{meas}

MAXIMUM MEASURABLE DIMENSION OF A PARTICLE

D_{min}

MINIMUM DIAMETER OF A PARTICLE IN A PSD 25

DPC

CLOUDSAT DATA PROCESSING CENTER

DPR

DUAL FREQUENCY PRECIPITATION RADAR

dr

SPATIAL DISTANCE

dt

TIME DIFFERENCE

DWR

DUAL WAVELENGTH RATIO

DWR_{min}

THE MINIMUM UNCORRECTED DWR ALONG A RADAR PROFILE

-E

REFERRING TO A SET OF EXPERIMENT-SPECIFIC RELATIONSHIPS

ECMWF

EUROPEAN CENTRE FOR MEDIUM RANGE WEATHER FORECASTS

ERAI

ECMWF REANALYSIS-INTERIM

GCPEX

GPM COLD SEASON PRECIPITATION EXPERIMENT

GPM

GLOBAL PRECIPITATION MEASUREMENT

GV

GROUND VALIDATION

HIWRAP

HIGH ALTITUDE WIND AND RAIN AIRBORNE PROFILER

HO

HORIZONTALLY ORIENTED

IOP

INTENSIVE OBSERVATION PERIOD

JJA

JUNE-JULY-AUGUST

L_f

LATENT HEAT OF FUSION FOR WATER

$m(D)$

MASS DISTRIBUTION

MAM

MARCH-APRIL-MAY

MC3E

MIDLATITUDE CONTINENTAL CONVECTIVE CLOUDS EXPERIMENT

MERRA

MODERN ERA RETROSPECTIVE ANALYSIS FOR RESEARCH AND APPLICATIONS

$n(D)$

SIZE DISTRIBUTION

NH

NORTHERN HEMISPHERE

noBB

NO BRIGHT BAND

Ob

Oblate

OLYMPEX

OLYMPIC MOUNTAINS EXPERIMENT

Orientation Distribution Function

Pr

Prolate

Q_{LW}

LONGWAVE HEAT FLUX

Q_{net}

NET OCEAN SURFACE HEAT FLUX

Q_{sen}

SENSIBLE HEAT FLUX

Q_{snow}

MELTING SNOW HEAT FLUX

Q_{SW}

SHORTWAVE HEAT FLUX

Q_{vap}

EVAPORATIVE HEAT FLUX

RO

Randomly Oriented

S

SNOWFALL RATE

SH

SOUTHERN HEMISPHERE

SON

SEPTEMBER-OCTOBER-NOVEMBER

-T

REFERRING TO A SET OF TEMPERATURE DEPENDENT RELATIONSHIPS

T_1

$-10 < T < 0$

T_2

$-20 < T < -10$

T_3

$-30 < T < -20$

T_4

$-40 < T < -30$

TRMM

TROPICAL RAINFALL MEASUREMENT MISSION

Z

REFLECTIVITY

Z_{Ka}

KA REFLECTIVITY

Z_{Ku}

KU REFLECTIVITY

CHAPTER 1 INTRODUCTION

1.1 MOTIVATION

Snow is a recurring form of precipitation across much of the planet for several months of the year. Snow that falls over land and ice changes the albedo of the surface, substantially impacting the radiative energy balance of the planet (Déry and Brown 2007). Snow defines the landscape for many biomes of the planet, and numerous species have evolved to occupy niches that require the regular accumulation of snowpack. When snow falls in higher latitudes, it can form seasonal snowpack or freeze into perennial glaciers. These mountain icepacks form "water tower" hydrology systems that represent the source of drinking water for over a billion people on the planet and the source of river water fundamental to whole ecosystems. At the most extreme latitudes, snowfall represents the dominating source of mass gain for the Greenland and Antarctic ice-sheets.

There is also a large amount of snow on the planet that is currently forming and falling through the atmosphere. This falling snow is important to understand for several reasons. Falling snow represents the beginning stages of over half of the precipitation on the planet (Field and Heymsfield 2015). Falling snow particles represent the biggest particles in frozen clouds, and they can bias the energy budget in climate models if they are not modeled appropriately (Waliser et al. 2011; Li et al. 2016a). Time-averaged measurements of falling snow can be used to verify climate and reanalysis models (Behrangi et al. 2016; Chen et al. 2016; Palerme et al. 2017b, a), and to measure snow precipitation in regions of the planet where direct measurements are scarce or impossible (Boening et al. 2012; Kulie et al. 2016; Liu 2009; Milani et al. 2018; Kulie and Milani 2018)

Falling snow is impossible to measure in the atmosphere directly, but it can be estimated from radar measurements. In locations that do not have surface radars, the only radar measurements come from satellites. There are three satellites that can measure falling snow: CloudSat, Tropical Rainfall Measurement Mission (TRMM) and Global Precipitation Measurement (GPM). Each of

these satellites have several outstanding limitations for conducting global snow research. CloudSat is the only satellite that takes measurements in polar latitudes, but it uses a thin W-band wavelength that is unreliable in moderate-to-heavy precipitation (Norin et al. 2015). The TRMM and GPM Ku band radars can measure the heaviest snowfall rates with no loss of accuracy, but they can *only* measure moderate-to-heavy snowfall rates; a high minimum detectable reflectivity leaves these radars blind to most frozen hydrometeors on the planet. Partially for these reasons, there have been few science applications of satellite precipitation radars to study research questions related to falling snow, even though these radars currently provide the only global information on falling snow.

1.2 OVERVIEW

In this dissertation, I study radar measurements that can retrieve snowfall information from satellite platforms.

In Chapter 2, I quantify the role of melting snow in the ocean surface heat flux using satellite measurements and atmospheric reanalysis models. This work was published in Geophysical Research Letters 2018, Volume 45 (Duffy and Bennartz 2018). Melting snow had previously been considered to be an unimportant contributor to the ocean surface heat flux. After converting global snowfall rates over oceans to heat transfers, I find that melting snow can theoretically become the largest heat flux during heavy snow storms and that it can represent a considerable fraction of the ocean surface heat flux during sea-ice formation and melting seasons.

In Chapter 3, I evaluate a novel retrieval of snowflake size from GPM measurements using experimental observations. This chapter provides the first empirically derived relationship between the dual-wavelength ratio and the mass-weighted mean diameter, parameters which are properly defined in Section 2. This research is in preparation for submission to the Journal of the Atmospheric Sciences with coauthors Ralf Bennartz, Greg McFarquhar, and Stephen Nesbitt.

In Chapter 4, I evaluate theoretical predictions of snowflake scattering and morphological properties, as well as the specific assumptions in the GPM precipitation retrieval algorithm,

through comparisons with the empirical relationship determined in the previous chapter. The main results from this chapter are that the measured relationship between DWR and D_m cannot be simulated based on the measured properties of snowflakes and that the relationship between DWR and D_m in the publicly provided GPM database is likely retrieving strongly biased properties of measured clouds.

CHAPTER 2 ESTIMATING THE ROLE OF MELTING SNOW IN THE OCEAN SURFACE HEAT BUDGET WITH CLOUDSAT SNOWFALL MEASUREMENTS

2.1 INTRODUCTION

2.1.1 MOTIVATION

Storms can have a profound effect on the high-latitude ocean surface energy budget. Across most of the Nordic seas, cold-air outbreaks are responsible for 60-80% of the turbulent heat flux in winter months (Papritz and Spengler 2017). The median estimates of turbulent flux under these storms vary from 250 to below 100 W/m^2, but in other parts of the world the most extreme cold-air outbreaks have been estimated to draw up to 2,500 W/m^2 of heat energy (Jensen et.al, 2011). The latent heat that dominates this turbulent heat flux is inherently linked to precipitation through the water cycle, and this precipitation has important thermodynamic implications in freezing regions: evaporation will lead to snowfall, and this snow will draw heat energy if it falls and melts into the ocean. While the energetic importance of ocean snowstorms have been discussed with respect to the radiative impacts of large cloud particles (Wolf et al. 2014; Waliser et al. 2011), there has not yet been any attention paid to the latent cooling implications of snow melting in the ocean, despite the fact that melting snow will draw 15% of the cooling energy of an identical volume of evaporating water. Since annual snowfall amounts are expected to decrease across the world's oceans as a consequence to climate change, It is important to understand the current state and significance of this cooling flux (Bintanja and Andry, 2017). Satellites provide a crucial role in researching this topic, as they provide the only global measurements of snow storms over ocean waters.

2.1.2 RESEARCH STATEMENT AND ORGANIZATION

In this study, I use satellite observations and climate reanalysis to quantify the role of melting snow in the ocean surface heat budget. In Section 2.2, I provide the equations required to calculate the heat flux from melting snow. In Section 2.3, I provide an overview of the data. In

Section 2.4 I provide results on the heat flux underneath individual storms, and in Section 2.5 I provide results on the average heat flux into the ocean on seasonal time scales.

2.2 THEORY

The ocean surface heat budget is modulated by the net ocean surface heat flux (Q_{net}),

$$Q_{net} = Q_{LW} + Q_{SW} + Q_{sens} + Q_{vap} + Q_{snow}$$

Equation 2-1

where Q_{LW} is the net longwave radiation flux, Q_{SW} is the net shortwave radiation flux, Q_{sens} *is* the sensible heat flux at the ocean-air boundary, Q_{vap} is the latent heat flux lost or gained from gas-liquid phase transitions, and Q_{snow} is the latent heat flux from melting snow. Q_{sens} is often approximated as

$$Q_{sens} = \rho_a c_p C_s U(T_s - T_a)$$

Equation 2-2

where ρ_a is the density of air, c_p is the specific heat capacity of air at constant pressure, C_s is the bulk transfer coefficient for sensible heat, T_s is the temperature at the water surface, U is the average wind speed, and T_a is the temperature of the air, assumed herein to be 2 meters above the ocean surface. Q_{vap} is approximated as:

$$Q_{vap} = \rho_a L_{vap} C_e U(q_s - q_a)$$

Equation 2-3

where L_{vap} is the latent heat of vaporization, C_e is the bulk transfer coefficient for latent heat, q_s is the specific humidity at the water surface, and q_a is the specific humidity of the air. q_s is estimated through the saturation specific humidity formula

$$q_s = 0.622 \frac{e_s}{P}$$

Equation 2-4

where P is surface pressure and e_s is the saturation vapor pressure, estimated through the Clausius-Clapeyron relationship

$$e_s = 0.6112 e^{\left(\frac{17.67 T_s}{243.5 + T_s}\right)}$$

Equation 2-5

Finally, Q_{snow} is calculated as

$$Q_{snow} = -L_f S$$

Equation 2-6

where L_f is the latent heat of fusion for water and S is the mass flux of melting snow. Snow can also provide a cooling flux through the temperature difference between frozen snowflakes and liquid water, but, for realistic temperature differences between a melting snowflake and the ocean water, back-of-the-envelope calculations prove this effect to be negligible compared to the latent heat of melting snow.

2.3 DATA

For the measurement of instantaneous heat fluxes, all values of Equation 1 are provided by the CloudSat Data Processing Center (DPC) or calculated from DPC products. CloudSat carries a W-band satellite radar which has been measuring reflectivity profiles of clouds and precipitation since its launch in 2006. DPC products use CloudSat and A-Train satellite retrievals alongside European Centre for Medium Range Weather Forecasts (ECMWF) atmospheric profile estimates to retrieve various atmospheric properties (Stephens et.al, 2002). Q_{LW} and Q_{SW} are provided in the CloudSat 2B-FLXHR-LIDAR data product (Henderson et.al, 2011). Cloudsat ECMWF-AUX (Partain, 2007) provides atmospheric variables of air temperature, specific humidity, and

pressure, and CloudSat 2C-PRECIP-COLUMN-R05 (Haynes et al., 2009) provides variables of sea surface temperature and wind speed, all necessary to calculate to calculate Q_{vap} and Q_{sens}. The CloudSat 2C-SNOW-PROFILE-R05 data product (Wood et.al, 2013, 2014) provides Bayesian estimates of surface snowfall rates with an a-posteriori retrieval uncertainty that varies between 150 and 250%. I set the instantaneous melting mass flux values of S for Q_{snow} equal to the liquid equivalent surface snowfall rates from the CloudSat 2C-SNOW-PROFILE-R05 data product (R05 was released in June 2018). This is a possibly biased assumption. Snowflakes might partially melt before they fall into the ocean, though previous studies that measure snowfall rates over the ocean typically ignore this effect (Behrangi et al. 2016). Snowflakes may also sublimate within the 500-100 meters between the ocean surface and the lowest retrievable radar bin, where radar contamination from surface interactions prevent meaningful precipitation retrieval. This could particularly be an issue for Southern Ocean snowstorms, where katabatic winds of low, dry air tend to partially or entirely dissolve coastal precipitation (Grazioli et al. 2017). Finally, it is conceivable that snowflakes deposited in the ocean may sometimes create a slush which would grow faster than it melted, delaying the cooling of the ocean and reducing the overall cooling flux from melting snow.

For measurements of seasonal snowfall, estimates from climate reanalysis models are used in place of CloudSat satellite measurements. Climate reanalysis combines global forecast models with measurements from multiple data-sources to adjust forecasts to witnessed phenomena. In this way, climate reanalyses provide a best estimate of global atmospheric properties for years when models and measurements are available. In regions where sea ice extent is variable, where annual snowfall tendencies can be determined by climate modes, or simply in mid-latitude oceans, the infrequent measurements of CloudSat often yield noisy and unsatisfying seasonal snowfall climatologies. Snowfall estimates from climate reanalyses have uniform grid cell coverage at most latitudes and can provide information on ocean snowfall for several decades before the launch date of CloudSat. I take advantage of the Arctic Observation and Reanalysis Integrated System (ArORIS) dataset, which provides collocated values of monthly averaged heat fluxes and precipitation rates from reanalyses and CloudSat at a 2.5° latitude and longitude scale (Christensen et al. 2016). In order to focus on open oceans where there is no additional flux from

melting or forming sea ice, monthly values for a coordinate are only considered when the sea ice fraction for that month is below 0.01.

While there are several global reanalysis models that provide snowfall estimates, ECMWF Reanalysis-Interim (ERAI) in particular has been recommended based on agreement with Cloudsat 2C-SNOW-PROFILE in reanalysis evaluations (Palerme et.al, 2014; Behrangi et al., 2016; Palerme et al., 2017). More recent results may dispute this corroboration, however. For example, another comparison of ERAI snowfall estimates with CloudSat in the Southern Ocean demonstrates relative differences in annual snowfall up to 50% (Milani et al. 2018) which were not seen in Behrangi et.al 2016. I find similar discrepancies between CloudSat and the Modern Era Retrospective analysis for Research and Applications (MERRA), a reanalysis model that has also been recommended for estimates of snowfall (Behrangi et al. 2016), in the NH . In the Southern Ocean, MERRA yields a much larger relative difference of snowfall rates compared to CloudSat estimates, and in the opposite direction. The highest resolution reanalysis snowfall estimates in the Arctic would come from the Arctic System Reanalysis version 2 (ASRv2; Bromwich et al., 2018), but only provides data over a limited domain and does not include the southern hemisphere. Snowfall estimates from ERAI are higher than those from ASRv2, generally yielding a 10-20% difference over oceans (Bromwich et al. 2018). Reanalysis models in general tend to suffer in high latitudes due to a scarcity of validating measurements, and noted biases in temperature that could impact the fraction of precipitation that is modeled to fall as snow. ERAI has been highlighted for agreements with independently measured temperatures and atmospheric variables in the Arctic (Chaudhuri et.al 2014; Jakobson et al., 2012). Results from Section 4.5 are presented in ERAI for this chapter.

2.4 INSTANTANEOUS HEAT FLUX

Figure 2.1 presents the median values of ocean surface heat fluxes underneath snow events ranked by snowfall rate. For clarity, the standard deviations of the range of Q_{SW}, Q_{LW}, Q_{vap}, and Q_{sens} about snowfall strength percentiles are not shown in the figure, but the associated values are 150-200, 10-20, 30-35, and 40-60 W/m^2, respectively. Q_{SW}, Q_{LW}, Q_{vap}, and Q_{sens} also carry

their own measurement uncertainties, but with over 50,000 retrievals included in each percentile, I assume these measurement uncertainties will converge. A second x-axis shows the ocean snowfall rates corresponding to selected percentiles. Because of the numeric value of L_f, a snowfall rate of 1.1 mm/h roughly corresponds to a cooling flux of 100 W/m^2, so snowfall rates can also be used to infer values of Q_{snow} when values are too low to resolve visually from the graph. Clearly, many snow events are not powerful enough to substantially impact Q_{net}. The lowest quartile of snow events barely draws 1 W/m^2 from the ocean, though it is debatable whether such low retrievals constitute or represent precipitation. The strength of snowstorms exponentially increases with decreasing likelihood, however, and Q_{snow} rapidly becomes an influential component of Q_{net} as snowstorms increase in strength beyond 0.1 mm/h.

Figure 2.1 is separated into daytime and nighttime storms. Snowstorms occur more often in long nights of cold seasons, but when Q_{SW} exists it tends to provide a dominating influence on all but the strongest snowstorms. The mostly increasing relationship between Q_{SW} and snowfall rate may seem counterintuitive, but natural changes of surface shortwave heating with seasons are one to two orders of magnitude greater than the attenuation from snowflakes (Waliser et al. 2011), so the curve of Q_{SW} is mostly mirroring that of top-of-atmosphere insolation. Apparently the majority of snow events tend to have higher snowfall rates during higher insolation, but the most powerful snowstorm events tend to occur most often during the lowest insolation, in winter months and/or at the highest latitudes. Another curious feature revealed by Figure 2.1 is the tendency for other cooling fluxes to minimize as Q_{snow} becomes more powerful. Some of this behavior can be expected from the natural preconditions of snowstorms: thicker clouds that emit downwelling longwave radiation minimize Q_{LW}, increased relative humidity near the surface under heavy precipitation decrease potential Q_{vap}, and decreased temperature gradients between the ocean and the atmosphere in heavy snow events decrease Q_{sens}. These explanations are not totally satisfying, however, as this trend is not consistent across the globe. Turbulent heat fluxes of Q_{sens} and Q_{vap} become weaker with increasing snowfall rate for snow events in the Northern Hemisphere (NH), while they are stronger and effectively constant for snow events in the Southern Hemisphere (SH). These differences might be owed to different types of snowfall events, but I are not yet certain why there is a difference between snowstorms in different hemispheres, or what other changes in curvature at tail ends of snowfall rates imply. A future

study that delves deeper into the nature of different kinds of ocean snowstorms in different locations and seasons could resolve these questions.

Based on Figure 2.1, Q_{snow} appears to be the dominant cooling influence in the ocean during the top 20th percentile of snowfall events. Considering that Cloudsat has noted limitations in retrieving snowfall rates above 1 mm/h when compared with surface radar (Norin et.al, 2015), it is likely that heavier snowfall rates which could lead to the most powerful cooling fluxes are undercounted. Further considering that calculations of Q_{snow} are based on an uncertain assumption that the satellite retrieved rate of snowfall will equal the rate of snowmelt, the exact threshold when melting snow could become the dominant cooling flux is not confident. With snowfall rates growing in strength exponentially as other heat fluxes tend to decrease towards zero, however, it is clear that my estimate of Q_{snow} rapidly becomes several times stronger than average values of other cooling fluxes during heavy snowstorms. Even considering possible Q_{snow} overestimates from idealized assumptions, these results demonstrate that melting snow will be a powerful heat flux contributor during many ocean snow events.

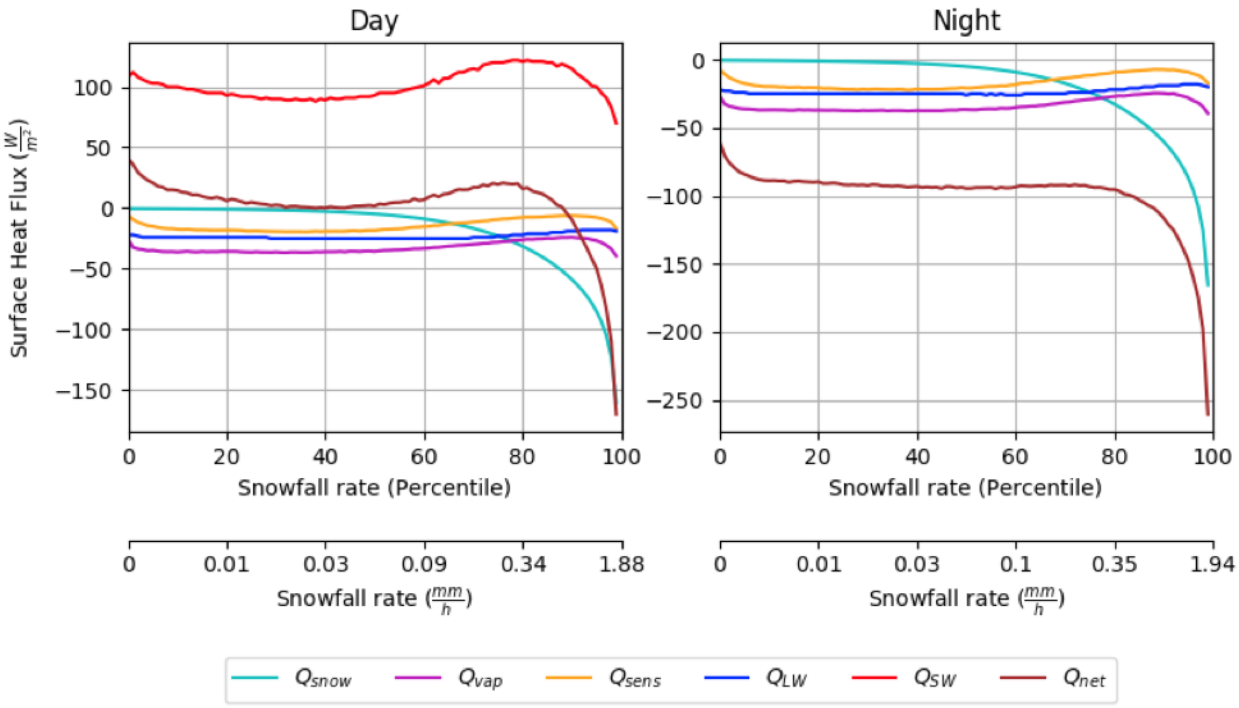

Figure 2.1
Median surface heat fluxes under ocean snowstorms, ranked by surface snowfall rate, separated into daytime and nighttime storms.

2.5 SEASONALLY AVERAGED HEAT FLUX

Figure 2.2 presents average Q_{snow} values for NH (top) and SH (middle) during the four meteorological seasons: December-January-February (DJF), March-April-May (MAM), June-July-August (JJA), and September-October-November (SON). Snowfall climatologies responsible for Q_{snow} tendencies are simple, and tend to follow broad symmetries. In the SH, average snowfall rates decrease northward from shorelines. In the NH, average snowfall rates are strongest directly to the south and east of shorelines, ultimately decreasing to zero in the northwest Pacific and Atlantic Oceans where temperatures remain warm enough for precipitation to fall as rain year-round. Average snowfall rates tend to be heavier in the SH; Q_{snow} is generally -1 – -3 W/m^2 stronger in the respective polar seasons of winter, autumn, and spring, and the SH annual average heat fluxes are roughly double those in the NH (bottom). The biggest difference

in the snowfall climatologies of the two regions comes in polar summer. In the SH, snowfall is weakest during DJF, but still substantial; close to annual averages of NH values. In the NH JJA, however, ocean snowfall amounts are scarcely above zero until past 75° N. Annual zonal averages of snowfall are fairly constant in the NH – tending between -1 and -2 W/m^2 past 50 °N – and J-shaped in the SH – decreasing from 0 to -4 W/m^2 between -50 and -60°, leveling off between -60 and -70°, and rising again to the coast.

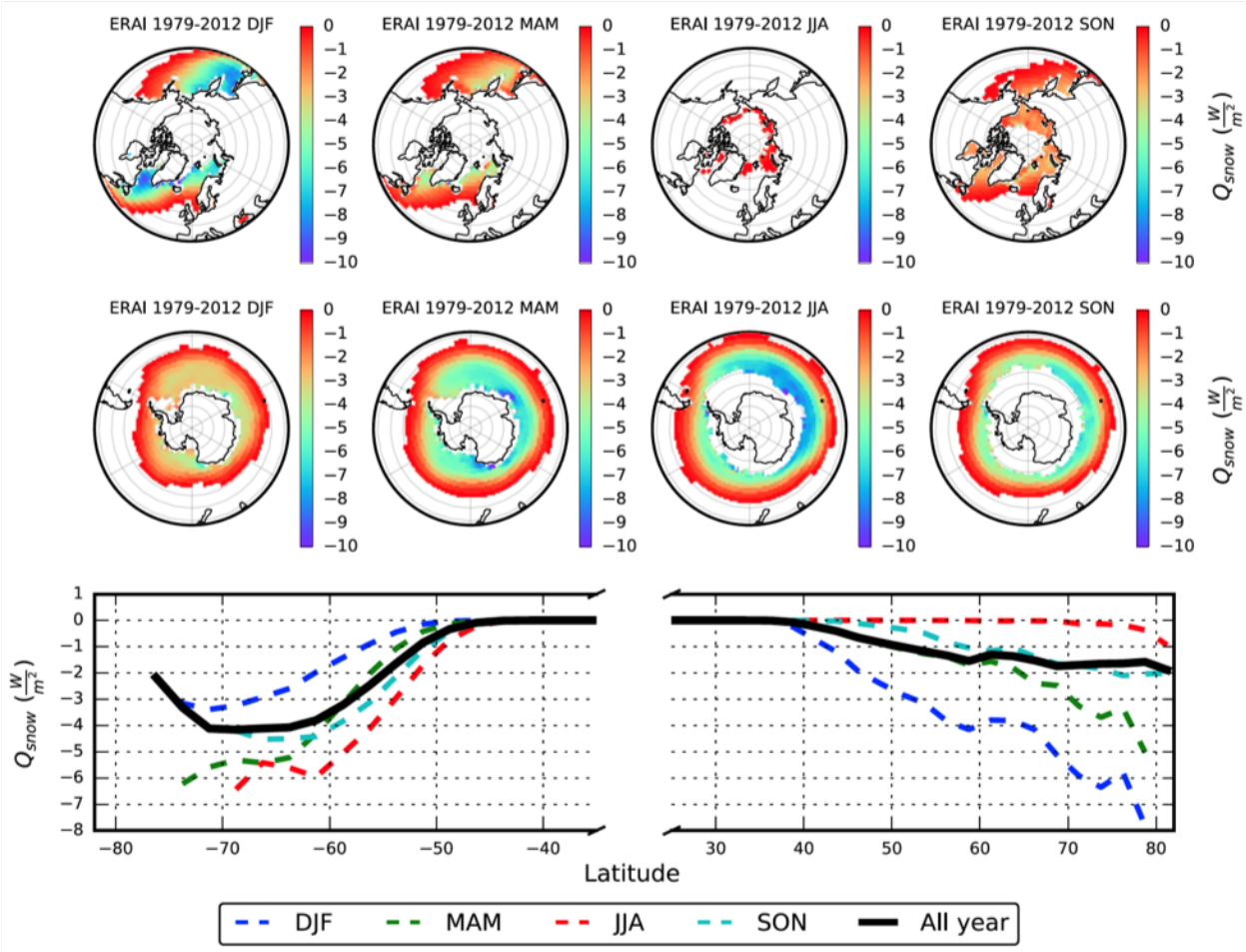

Figure 2.2
Seasonal average values of QSNOW, presented as gridded averages in the NH (top row), SH (middle row), and as zonal averages across the entire planet (bottom row). Annual zonal averages are also presented. NH = Northern Hemisphere; SH = Southern Hemisphere; ERAI = ERA-Interim; DJF = December, January, February; MAM = March, April, May; JJA = June, July, August; SON = September, October, November.

Seasonal average values of Q_{snow} are low, but not too far below ocean turbulent heat fluxes at high latitudes, which tend to have annual averages between -20 and -50 W/m^2 (Smith, et.al, 2011; Sorteberg et.al, 2007). Especially considering the fact that the warming flux Q_{SW} acts in opposition to the cooling fluxes of Q_{LW}, Q_{sens}, and Q_{evap}, Q_{snow} could become influential when Q_{net} becomes balanced and approaches 0. In order to explore the importance of Q_{snow} with respect to the average net ocean heat budget, I define a Snowfall Impact Metric (*SIM*) as

$$SIM = 100 \times \left(\frac{|Q_{snow}|}{MAX(|Q_{net}|, |Q_{snow}|)} \right)$$

Equation 2-7

and map this metric for every year in the ArORIS ERAI record. The metric is made bipartite in order to ensure that the metric does not diverge when Q_{net} approaches zero. Whenever the absolute value of Q_{SNOW} is larger than the absolute value of Q_{NET}, SIM yields on a percentage scale the relevance of Q_{snow} relative to Q_{net}. If $|Q_{NET}|$ is smaller than $|Q_{SNOW}|$, SIM will result in SIM = 100% (but not exceed 100%), indicating that the magnitude of Q_{SNOW} is as large as Q_{Net} or larger.

Figure 2.3 presents SIM averaged across the Northern and Southern hemispheres between 1979 and 2012. Regions with substantial values of SIM indicate areas where Q_{snow} may play an influential role in the ocean heat budget on seasonal time scales. It is important to note that, since Figure 2.3 represents the average value of SIM, similar values can represent different ocean heat budget behavior. Specifically, the SIM values in the Southern Ocean during JJA are the result of a consistent average value of 5-10%, while the SIM values in the Atlantic and Pacific are the result of wider inter-annual variations between 0 and 50%. In general, SIM values are broader and more consistent in the SH, while they are more varied and heterogeneous in the NH.

According to Figure 2.3, Q_{snow} barely appears to make a large difference in the ocean heat budget globally in JJA or DJF months, despite the fact that Q_{snow} is strongest in polar winter. Clearly, the lack of sunlight and large differences between water surface and air temperature all lead to turbulent and radiative cooling fluxes that dwarf any contribution from snow. During

MAM and SON however, there are ocean regions with SIM values between 20% and 30%, indicating a substantial influence from melting snow. Wide regions of the high latitude Pacific, Atlantic, and Southern oceans are noticeably impacted by melting snow, even though Q_{snow} in these seasons often average just a few W/m^2. Some of the strongest and most consistent SIM values appear in the highest latitude Arctic and Southern Oceans during SON and MAM, respectively. These regions represent waters that are only ice-free for a few months of a year, and in the Arctic Ocean, waters that have only begun melting seasonally within the past few decades. Q_{snow} may therefore play an important role during critical periods of sea-ice recovery in climate-sensitive oceans.

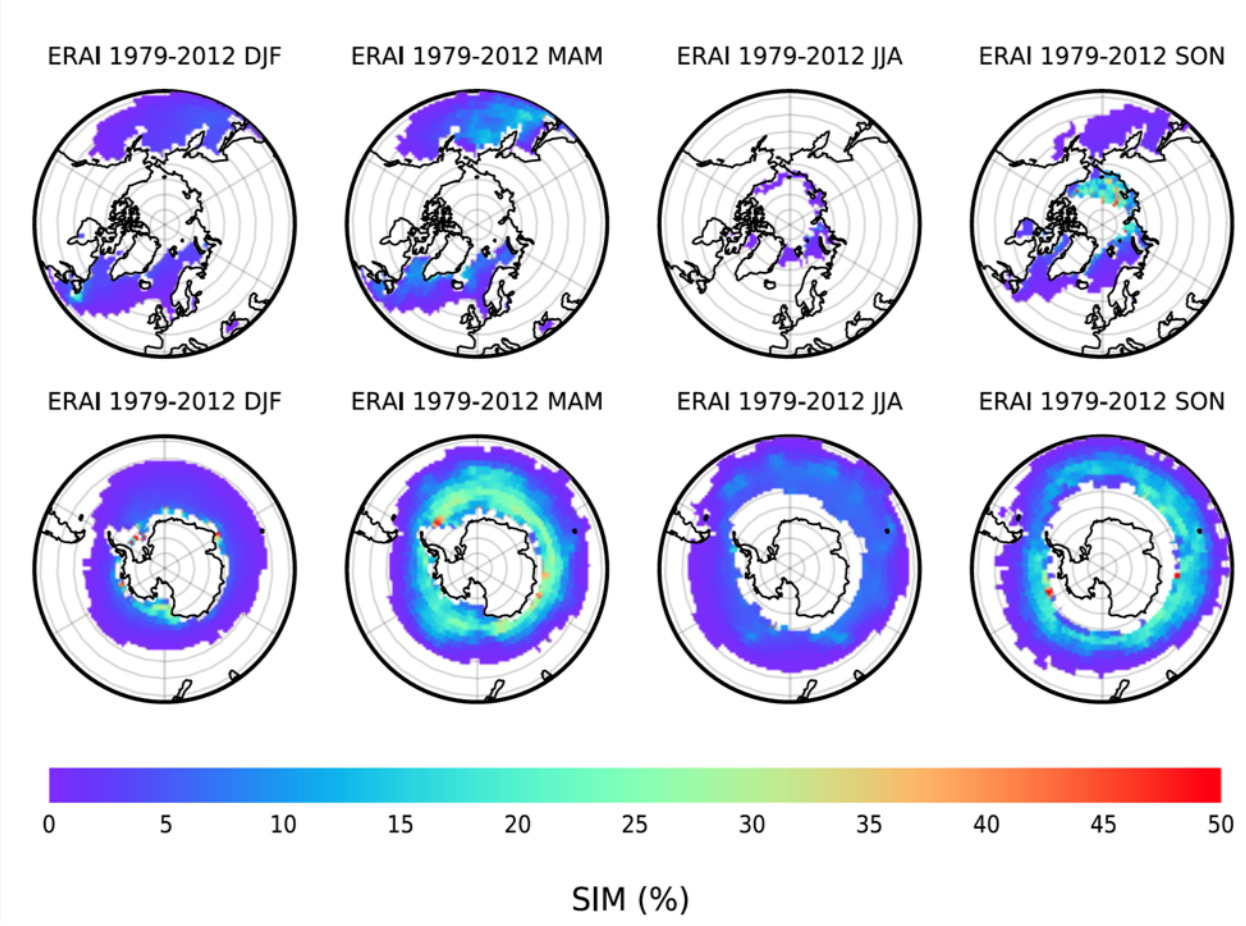

Figure 2.3
Seasonal averages of SIM in the NH (top row) and SH (bottom row). SIM = Snowfall Impact Metric; NH = Northern Hemisphere; SH = Southern Hemisphere; ERAI = ERA-Interim; DJF = December, January, February; MAM = March, April, May; JJA = June, July, August; SON = September, October, November.

2.6 CONCLUSION

Snow is a regular experience for many of the world's oceans, and as it melts it draws heat energy from the ocean's surface. Intuitively, the impact of melting snow in the overall ocean surface heat budget may seem inconsequential; snow affects a minority of the world's ocean during a small part of the year with a fraction of the cooling potential of the latent heat of vaporization for an identical volume of water. Through satellite measurements and reanalysis estimates, however, I find that the cooling influence of melting snow can often be relatively important. The cooling flux from melting snow is often on the order of radiative and turbulent cooling fluxes for snowstorms with snowfall rates greater than 0.1 mm/h, roughly 40% of the snow events in the world. Melting snow is likely most powerful heat flux in the ocean surface during particularly intense snowstorms.

The influence of melting snow is important on longer time scales as well. Using snowfall estimates from ERAI, I find that seasonal cooling fluxes can be as low as -10 W/m^2 off high latitude coastlines in winter, though it is much more often between 0 and -6 W/m^2 depending on season and latitude. The impact of melting snow in the ocean heat budget is largest in the Western Pacific and Atlantic oceans in MAM and in the Southern Ocean in MAM and SON. Melting snow also appears influential in the heat budgets of high latitude Arctic and Southern oceans during SON and MAM, respectively, indicating a possible importance of melting snow in ocean thermodynamics during sea-ice freezeup.

With warmer temperatures from climate change disproportionately affecting high latitude regions, snow events over the ocean will soon become less frequent, being replaced with rain events that do not provide a latent cooling flux. Especially in regions where Q_{snow} makes up a large component of the seasonal ocean surface heat flux, this loss of cooling energy may impact calculations of future sea ice and ocean dynamics. Estimates of snowfall over oceans are still uncertain in models and measurements, so when there is a difference between the two it can not be certain which one is closest to the truth. It is likely that ERAI and/or CloudSat estimates of snowfall are biased by up to 50% in the Southern Ocean (Milani et al. 2018), which could impact

the Q_{snow} values in Sections 2 and/or 3 by large margins. Outstanding questions of snow sublimation and melting in the surface clutter zone and reflectivity-snowfall rate relationship validations over oceans will need to be addressed to improve my understanding of snowfall over the ocean and the influence of melting snow in the ocean heat budget.

CHAPTER 3 EMPIRICAL RELATIONSHIPS BETWEEN DUAL FREQUENCY RADAR MEASUREMENTS AND MASS-WEIGHTED MEAN DIAMETER IN FROZEN PRECIPITATION

3.1 INTRODUCTION

3.1.1 MOTIVATION

Section CHAPTER 2 provided one example of the kind of unique and valuable information that satellite snowfall measurements can provide for the Earth's climate. GPM does not have a polar orbit and it cannot detect the majority of falling snow events, so it is not as capable of providing similar information. The Dual Frequency Precipitation Radar (DPR) on board the GPM does, however, hold the potential for the most powerful and novel observation of frozen precipitation above rain clouds currently possible. This observation comes through the Dual Wavelength Ratio (DWR)

$$DWR = 10log_{10}(Z_1) - 10log_{10}(Z_2)$$

Equation 3-1

, with Z_1 and Z_2 representing reflectivities with different wavelengths, assumed herein to be the Z_{Ku} and Z_{Ka} measurements of the DPR. DWR is predicted to have a strong relationship to the mass weighted mean diameter, or D_m, defined as

$$D_m = \frac{\int_{D_{min}}^{D_{max}} n(D)m(D)DdD}{\int_{D_{min}}^{D_{max}} n(D)m(D)dD},$$

Equation 3-2

with $m(D)$ representing a mass distribution, $n(D)$ representing a measured or modeled particle size distribution (PSD), D representing a one-dimensional measurement of particle size, and D_{min} and D_{max} representing the largest and smallest particles considered for the PSD. D_m is a fundamental parameter which determines the size distribution of precipitation in retrieval

algorithms. Single wavelength reflectivity (Z) has a relationship to D_m, but Z is also influenced by snowflake mass and concentration. DWR is predicted to be largely insensitive to changes in concentration, density, or particle shape (Liao et al. 2005), leading to an expectedly superior retrieval of D_m in global measurements of diverse clouds compared to Z. A comparison of empirical relationships between DWR, Z, and D_m from different environments can confirm or refute this prediction.

3.1.2 RESEARCH STATEMENT AND PROCEDURE

The goal of this study is to answer three research questions: "What is the relationship between DWR and D_m in clouds, and how does it compare to the relationship between Z and D_m?", "How do the relationships between radar measurements and D_m vary between different environments?", and "Does the DWR-based D_m retrieval method provide more accurate and consistent results than a Z-based D_m retrieval method?". For the purposes of this study, "environments" refers to cloud types (e.g., convective or stratiform), storm types (e.g., synoptically forced or lake-effect), cloud temperature, and storm location.

To answer these questions, we generate a large dataset of collocated reflectivity and D_m from three different GPM Ground Validation (GV) experiments: the GPM Cold Season Precipitation Experiment (GCPEX; Skofronick-Jackson et al., 2015), the Midlatitude Continental Convective Clouds Experiment (MC3E; Jensen et al., 2016), and the Olympic Mountains Experiment (OLYMPEX; Houze et al., 2017). GCPEX studied precipitation in winter snowstorms, including lake effect snow. It was conducted from January through February 2012 near Barrie, Ontario. MC3E studied precipitation in springtime convective storms. It was conducted from April through June of 2011 near Lamont, Oklahoma. OLYMPEX studied precipitation in winter orographic storms. It was conducted from November through December 2015 near and offshore of the Olympic Peninsula in Washington over and surrounding the Olympic Mountains. Periods during experiments when the aircraft were sampling storms are referred to as "Intensive Observation Periods," or IOPs. During these IOPs, at least one airplane with a radar flew above clouds, while another airplane carrying *in-situ* probes conducted measurements inside of

clouds. Collocated measurements refer to periods of time when the two planes were sampling similar volumes.

IOPs in this study are denoted according to the first letter of the experiment, followed by two numbers representing the month, and two numbers representing the day. For example, the OLYMPEX December 1st IOP is referred to as "O1201". A depiction of the flight patterns that provided collocated measurements for this IOP is provided in Figure 3.1.The process used to match *in-situ* and reflectivity measurements to the same time series is described in Section 3.2. The functions used to derive empirical relationships are described in Section 3.3. The results of the study are presented in Section 3.4 and discussed in Section 3.5.

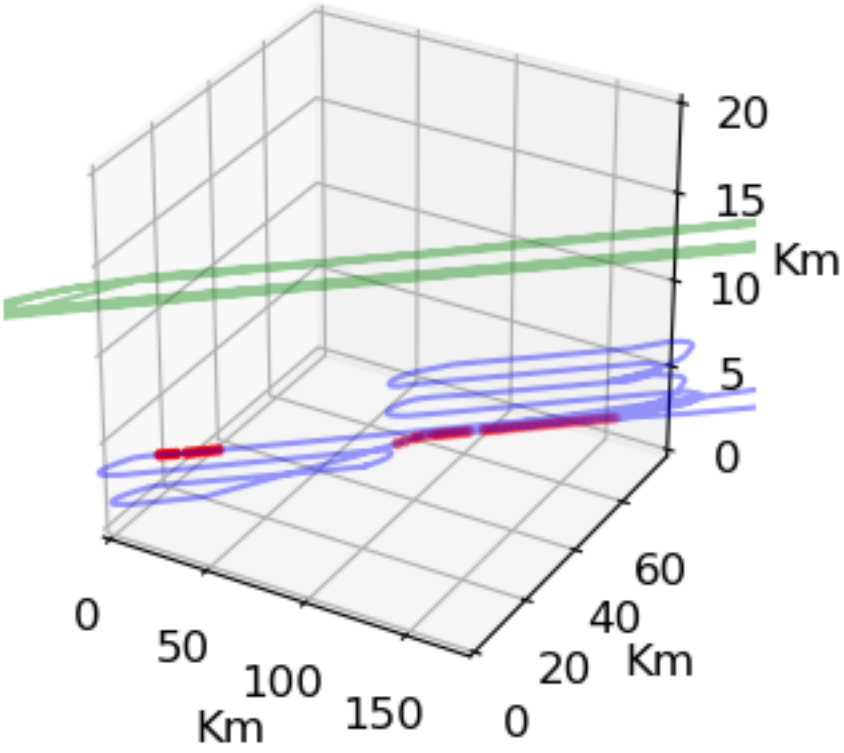

Figure 3.1
Flight paths of a radar aircraft (green) flying above an *in-situ* aircraft (blue) during the O1201 IOP. *In-situ* measurements that are collocated with radar measurements are highlighted in red (See Section 2 for the definition of "collocated" used in this study.)

3.2 GENERATING A MATCHED D_M – DWR DATASET

3.2.1 D_M MEASUREMENTS

D_m is calculated from measured PSDs through Equation 2. PSDs were derived from one-dimensional sizes of imaged snow particles (D_{meas}) by the National Center of Atmospheric Research (NCAR) at 1 s resolution. To make the results of this study comparable to NASA-retrieved GPM measurements of D_m, liquid equivalent diameters of snow particles (D_{liq}) - referring to the diameter of a liquid drop with the same mass as a measured or simulated snow particle - are preferred for calculations of Equation 2. D_{liq} is related to D_{meas} through

$$D_{liq} = \left(\frac{6a}{\rho_w \pi}\right)^{\frac{1}{3}} {D_{meas}}^{\frac{b}{3}},$$

Equation 3-3

where ρ_w represents the density of water and a and b represent the mass coefficient and exponent parameters used to estimate the mass of a snow particle through a power-law mass distribution

$$m(D_{meas}) = a{D_{meas}}^{b}.$$

Equation 3-4

This is not to be confused with the mass distribution for D_{liq} necessary to calculate D_m from Equation 2, defined as

$$m(D_{liq}) = \rho_w \frac{D^3}{6}.$$

Equation 3-5

For the rest of this paper, D inherently refers to $D_{liq.}$ Snow particles are assumed to follow the Heymsfield et al. (2010) mass distribution of a = 0.007 g cm$^{-2.2}$ and b = 2.2 for frozen particles in unspecified convective or stratiform clouds.

D_{meas} is defined in image processing algorithms as the maximum measured dimension in any direction for a completely imaged snowflake, or the maximum measured dimension in any direction of a reconstructed image for a partially imaged snowflake (Heymsfield and Parrish 1978). PSDs were constructed drawing $D_{meas} < 1$ mm from 2-Dimensional Cloud Imaging Probe (2D-C), 2D Stereo (2D-S), or Cloud Imaging Probe (CIP) images and $D_{meas} > 1$ mm from High-Volume Precipitation Spectrometer 2 or High Volume Precipitation Spectrometer 3 (HVPS2, HVPS3) images. Probes used to image particles in different experiments are listed in Table 1. The PSDs collected during an example IOP are visualized in Figure 3.2.

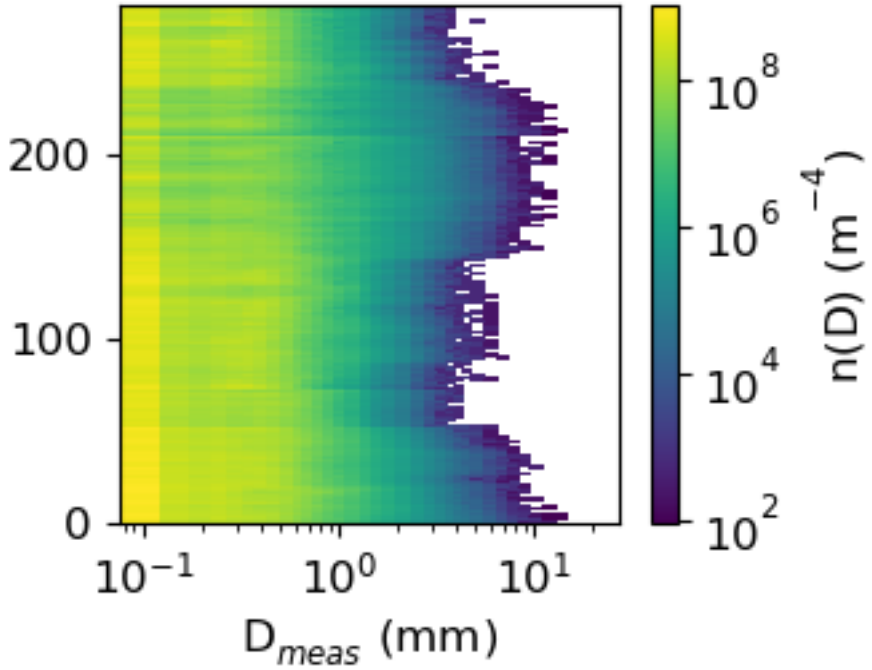

Figure 3.2
PSDs from the M0520 IOP that are used in this study

3.2.2 DWR MEASUREMENTS

Radar measurements either come from the High Altitude Wind and Rain Airborne Profiler (HIWRAP; Li et al., 2016) radar, which was deployed on the NASA ER-2 high altitude aircraft, or the Advanced Precipitation Radar (APR; Sadowy et al., 2003) 2 or 3, which was deployed on

the DC-8 aircraft. Radars used in different experiments are listed in Table 3.1. The HIWRAP was set up to provide collocated Ku/Ka reflectivities at a nadir scan for GV experiments. The HIWRAP has nominal Ku and Ka frequencies of 13.9 and 35.6 GHz, respectively. The HIWRAP has a minimum detectable reflectivity of 0 and -5 dB at Ku and Ka wavelengths, respectively. The APR 2 and APR 3 contain Ku and Ka scanning radars with nominal frequencies of 13.4 and 35.6 GHz respectively, though just the nadir pointing Ku and Ka reflectivity scans are used in this study. The APR has minimum detectable reflectivities of 5 dB at both Ku and Ka wavelengths. Initial radar gate widths were 30 m wide for APR measurements, 37 m wide for HIWRAP during OLYMPEX, and 75 m wide for HIWRAP during MC3E. Radar range gates were smoothed along radar profiles with an approximately 250 m boxcar average in mm^6m^{-3} units to have a similar resolution to the DPR.

Experiment	Radars	Imaging probes
GCPEX	APR2	2DC, CIP, HVPS2
MC3E	HIWRAP	2DC, CIP, HVPS2
OLYMPEX	APR3, HIWRAP	2DS, HVPS3

Table 3.1
Radars and imaging probes used during each experiment

Sources of DWR unrelated to D_m could have a negative influence on the empirical relationships. Attenuation – the decrease of measured reflectivity due to radiation absorption from water and atmospheric gasses – is stronger at Ka band than Ku, and can increase a measured DWR along a radar path. Independently varying Ku and Ka radar noise combine to form random DWR errors inside of clouds, and differences between Ku and Ka radar sensitivities lead to DWR artifacts along the tops of clouds. Ku and Ka components of the HIWRAP and APR also experience independent calibration errors, and any differences in these errors will uniformly bias DWR measurements. With the exception of cloud-edge artifacts, which can be very large but are easily identifiable and removed, these errors should be relatively minor. Calibration errors should be on the order of 1 or less dB. Supercooled liquid water that could cause attenuation along a radar profile is unmeasurable, and is therefore considered as a possible source of error. This effect has previously been considered ignorable for Z_{Ka} measurements through orographic and

stratiform snow clouds (Chase et al. 2018; Matrosov 2007), but these assumptions may not apply for DWR snow retrievals through convective clouds.

The procedure used in this study to identify and remove DWR not related to D_m is depicted through a series of subplots in Figure 3.3. The DWR presented in Figure 3.3a has already received the 250 m weighted average, reducing some of the random DWR error. Since attenuation and D_m will both increase along a radar path due to increasing liquid water pathand the growth of snowflakes, the DWR related to these processes will tend to be minimized at cloud-top. Any consistent non-zero DWR at cloud-top should be a fair representation of calibration error, but since DWR artifacts visibly dominate cloud-top reflectivity, the minimum DWR along a radar profile (referred to as DWR_{min} for the remainder of this section) is used instead (Figure 3.3b).

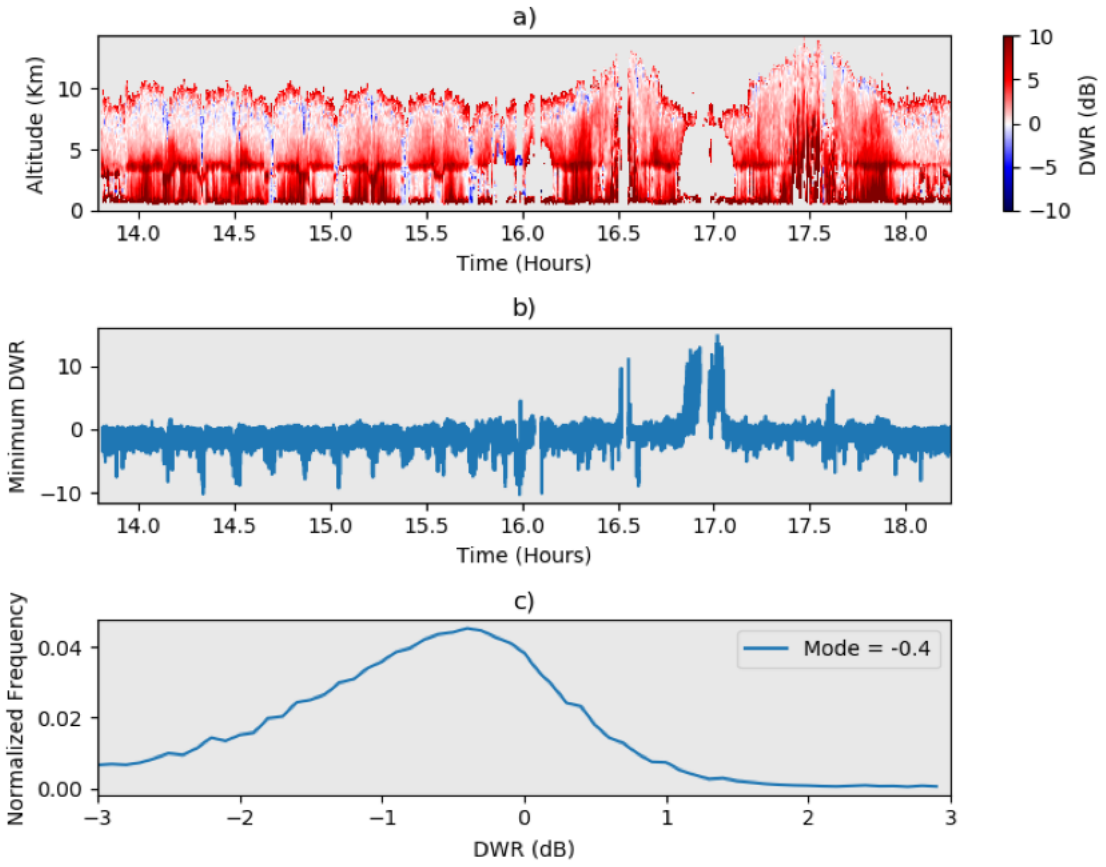

Figure 3.3
A visual depiction of calibration bias identification during M0520. Figure 3a displays a time series of vertical profiles of the DWR reflectivity. Figure 3b displays the time series of DWR_{min} along vertical profiles. Figure 3c displays a histogram of the DWR_{min} from Figure 3b, with the mode provided in the legend.

As visible in Figure 3.3, the time series of DWR_{min} has a visibly consistent offset throughout M0520. This consistency is evident for all IOPs used in this study, indicating that a single value can be used to debias DWR measurements during an IOP. The distribution of DWR_{min} is displayed in Figure 3.3c, and the mean, mode, and standard deviation of DWR_{min} for each IOP are shown in Table 3.2. The mode of DWR_{min} values is used as the DWR offset to avoid the influence of high DWR_{min} outliers, visible in Figure 3.3a and Figure 3.3b near 17 h. DWR offsets from Table 3.2 are subtracted from all DWR measurements.

IOPs	Mode (mm)	Mean (mm)	Standard Deviation (mm)
G0212	1.03	1.45	1.35
G0224	0.24	1.65	1.44
M0425	0.01	2.36	4.25
M0520	0.17	0.20	0.86
M0523	-0.52	0.12	2.48
O1201(HIWRAP)	0.23	0.37	0.81
O1212 (HIWRAP)	0.28	1.13	1.86
O1201 (APR)	0.16	0.52	0.79
O1212 (APR)	0.23	0.73	0.91
O1218 (APR)	0.20	0.73	0.97

Table 3.2
Mode, mean, and standard deviations of DWR_{min} for each experiment

3.2.3 TEMPORAL AND SPATIAL MATCHING.

A nearest-neighbor algorithm is used to join the radar and in-situ measurements to the same time series; the closest horizontal point of reflectivity is matched to the Citation's location for every second of flight time. Matched *in-situ* and radar measurements are averaged into discrete 10 s intervals, corresponding to an *in-situ* measurement path of little more than a kilometer. Data are then excluded if the spatial distance (dr) and time difference (dt) between the *in-situ* and radar observations fall beyond chosen boundaries. dr and dt are chosen on the basis of a sensitivity test that determine the number of IOPs, the number of total data points, and the average rank correlation coefficient ($\bar{\rho}$) between DWR and D_m at different dr and dt (Figure 3.4). ρ is chosen as the correlation coefficient since it can be used to identify non-linear relationships between two variables, and the relationship between DWR and D_m is predicted to be non-linear across the full span of measured DWR (Liao et al. 2016). $\bar{\rho}$ represents the average of correlation coefficients among individual IOPs, not to be confused with the correlation of the combined data set. IOP data is only incorporated into Figure 3.4 if it displays a statistically significant ρ, here considered to have a corresponding $p < 0.01$ (99% statistically significant), and provides more than five measurements. There is a broad region where all IOPs have $p < 0.01$, meaning all data sets provide statistically significant relationships between DWR and D_m. This region is shaded in black in Figure 3.4a, and only values within this region are considered. $\bar{\rho}$ is broadly similar under

a wide range of thresholds until there is a general drop with increasing dr and dt after dt > 3.5 min and dr > 12 km. “Collocated data” is accordingly defined with a dr and dt of 12 km and 3.5 min, respectively.

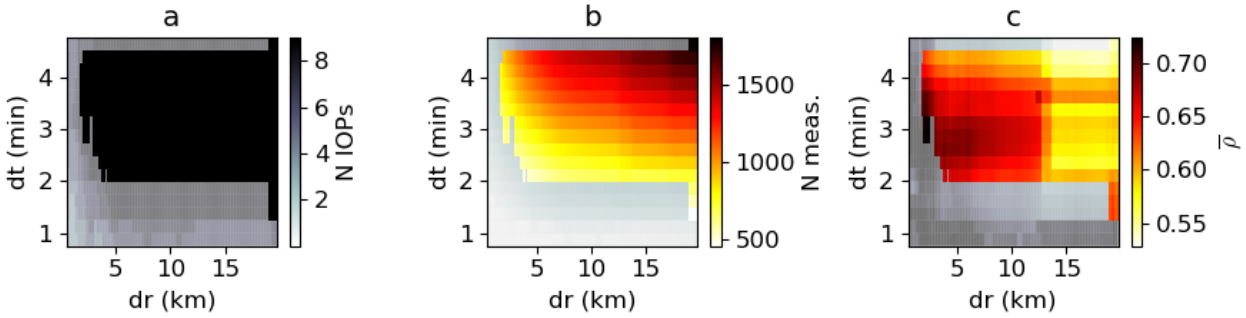

Figure 3.4
Number of IOPs (N IOPs; 2a), number of measurements (N meas.; 2b) and average rank correlation coefficient (ρ; 2c) resulting from every presented combination of dr and dt thresholds.

Any data with dt less than 10 s is removed to eliminate the possibility of reflection from the aircraft being included in the dataset. Data is removed if the temperature is warmer than -3°C to remove liquid precipitation and melting snow. An example of the final collocated data, demonstrating the approximate location of the Citation during radar measurements and the time series of collocated DWR and D_m data during G0224, is presented in Figure 3.5.

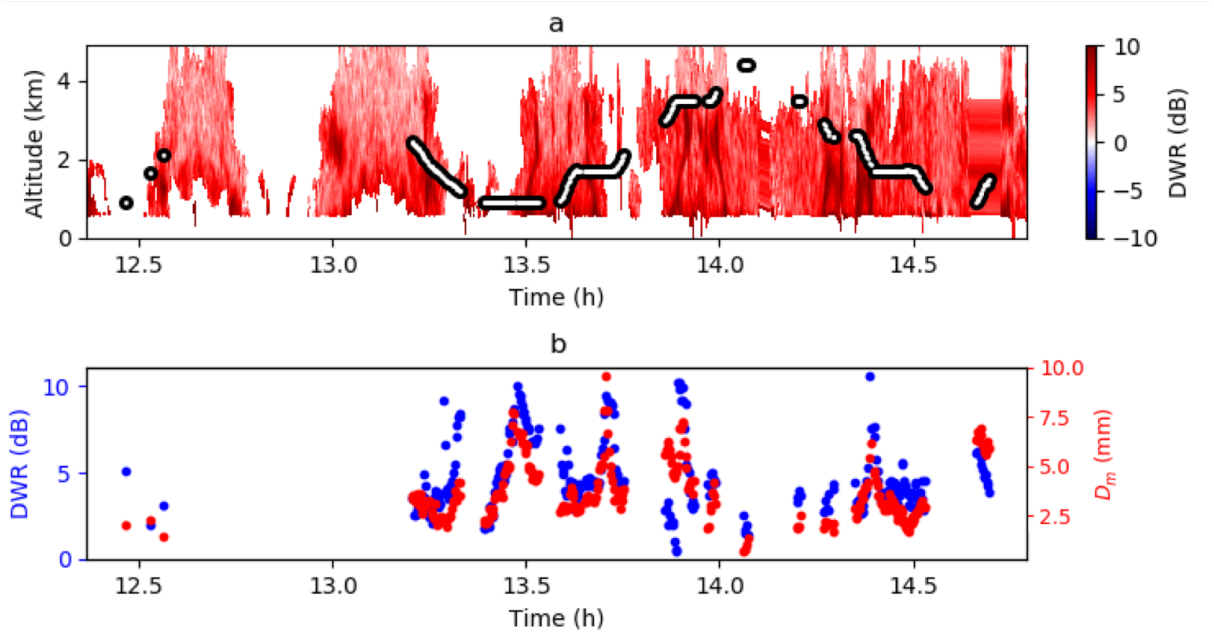

Figure 3.5
3a shows the measured DWR reflectivity during G0224, with in-situ altitudes during collocated measurements laid on top. 3b shows the DWR and Dm matched to the same time series.

3.3 FIT FUNCTIONS FOR EMPIRICAL RELATIONSHIPS

Measured relationships between Z and D_m (or its inverse counterpart, Λ) have been observed to follow a power law (Matrosov and Heymsfield 2017; Skofronick-Jackson et al. 2019). The same convention is followed in this study, with

$$D_m(Z_{Ku}) = c_1 {Z_{Ku}}^{c_2}$$

Equation 3-6

Z has units of $mm^{-6}m^{-3}$ in Equation 6, but in the results it is plotted with units of dBZ.

The relationship between DWR and D_m has not been observed before this study, but it has been simulated by applying scattering models to model size distributions. Three simulated relationships resulting from different scattering models are presented in Figure 3.6. Reflectivity is calculated as

$$Z_\lambda = \frac{\lambda^4}{K_w(\lambda)^2 \pi^5} \int_{D_{min}}^{D_{max}} n(D)\sigma_b(D)dD$$

Equation 3-7

with K_w representing the Clausius-Mossotti expression for the dielectric constant of water, $\sigma_b(D)$ representing the backscattered cross-section distribution of snow particles and, λ representing the radar wavelength. The dendrite aggregate and needle aggregate models are simulated through the Self-Similar Rayleigh Gans Approximation, with habit specific parameters drawn from Mason et al. 2019. Spheroid models are calculated with PyTmatrix (Leinonen 2014), incorporating the shape and orientation parameterizations for ice particles from Hogan et al. (2012). All simulated relationships follow the Heysmfield et al. 2010 mass parameterization used throughout this study, and snow PSDs are represented by an exponential function (Heymsfield et al. 2008; Liao et al. 2016; Borque et al. 2019)

$$n(D) = N_0 e^{-\frac{4}{D_m}D}$$

Equation 3-8

, with N_0 representing the intercept parameter. The parameterization of N_0 is inconsequential for calculations of DWR and D_m, and D_m is set to the range witnessed in the GV experiments.

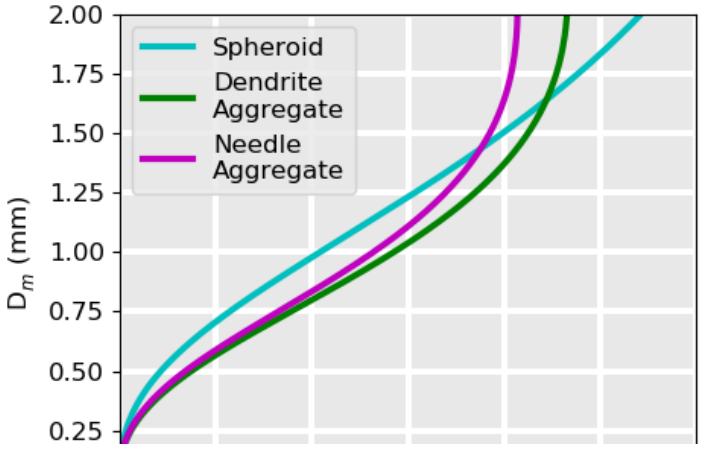

Figure 3.6
Simulated relationships between DWR and Dm generated from different scattering models

The simulated relationship is characterized with an origin at 0, a negative curvature at lower DWR, and a positive curvature at high DWR. The D_m where positive curvature begins varies with different scattering models. Both dendrite and needle aggregate scattering models begin to gain a positive curvature after D_m exceeds 1 mm, and they are both defined by near-vertical slopes after $D_m = 1.75$, but these vertical slopes are associated with different maximum DWR (8 dB and 9 dB for needle aggregates and dendrite aggregates, respectively). The spheroid curve barely shows any sign of positive curvature within the figure bounds, which represent the range of measured data.

To allow for the change of inflection, a second power law is added for the $D_m(DWR)$ regression function. In practice, an odd function that predicts negative values for D_m is necessary to ensure that the average of random DWR noise about zero leads to a 0 mm D_m. The complete form of the DWR-D_m empirical relationships is presented as

$$D_m(DWR) = \begin{cases} c_3 DWR^{c_4} + c_5 DWR^{c_6}, & DWR >= 0 \\ -c_3|DWR|^{c_4} - c_5|DWR|^{c_6}, & DWR < 0 \end{cases}$$

Equation 3-9

DWR remains in units of dB in Equation 9. To ensure the function follows the desired shape, Equation 9 is bounded with $c_1 > 0$, $0.25 < c_2 < 1$, $c_3 > 0$, and $c_4 > 1$. 0.25 is a lower boundary for c_2 to prevent the term from minimizing to zero and simulating a non-physical y-intercept in the results. In certain results where high-influence outliers or small ranges of DWR led to visibly inappropriate overfitting, c_3 and c_4 were set to 0.

3.4 RESULTS

3.4.1 EMPIRICAL RELATIONSHIPS BETWEEN REFLECTIVITY AND D_M

The first set of results addresses the questions "What is the relationship between DWR and D_m in clouds?" and "How does it compare to the relationship between Z and D_m?" The different measured relationships between radar measurements and D_m are presented in Figure 3.7. Constants that define the three empirical relationships are provided in Section 3.4.2.

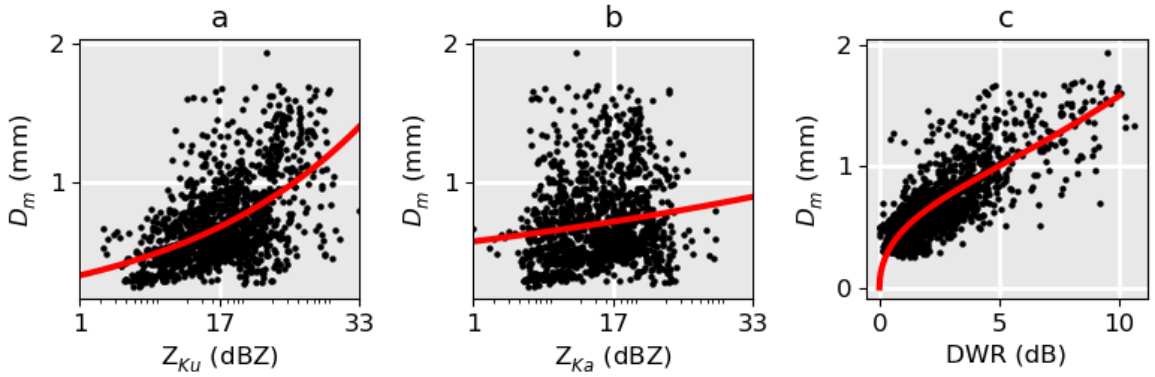

Figure 3.7
Scattered data and fit functions from the combined data set with respect to Z_{Ku} (a), Z_{Ka} (b), and DWR (c)

The scattered Z_{Ku} and D_m data form a wedge shape. Maximum D_m values increase from 0.75 to 2 mm with increasing Z_{Ku}, but minimum D_m values are relatively constant at 0.25 mm for all but the highest Z_{Ku}. The scattered Z_{Ka} and D_m display no visible correlation. The scattered DWR and D_m data display a visibly linear relationship with a similar thickness about the central regression across all DWR values. The linear region of the DWR-D_m relationship exceeds the boundary of maximum DWR for the simulated heterogeneous scattering models. The correlation between DWR and D_m is highest ($\rho = 0.77$), followed by Z_{Ku} and D_m ($\rho = 0.52$), and the correlation between Z_{Ka} and D_m is the lowest ($\rho = 0.3$).

3.4.2 SENSITIVITY OF EMPIRICAL RELATIONSHIPS TO DIFFERENT ENVIRONMENTS

The second set of results addresses the question "How do the relationships between radar measurements and D_m vary in different environments?". Most results in this section refer to scatterplots and empirical regressions of radar measurements and D_m from different subsets of the matched dataset. D_m, Z_{Ku}, Z_{Ka}, and DWR all tend to have different ranges for different data

subsets, and the ranges of these properties for different subsets are provided alongside regression function constants, the number of measurements, and correlation coefficients in Table 3.3, **Error! Reference source not found.**, and Table 3.5. Empirical relationships for different data subsets are only plotted within the ranges where radar data is represented.

	c_1 (Z_{Ku})	c_2 (Z_{Ku})	c_1 (Z_{Ka})	c_1 (Z_{Ka})	c_3	c_4	c_5	c_6
all	0.32	0.19	0.56	0.06	0.43	0.25	0.06	1.17
GCPEX	0.43	0.18	0.53	0.18	0.59	0.25	0.01	1.65
MC3E	0.37	0.11	0.43	0.07	0.42	0.27	0.04	1.00
OLYMPEX	0.29	0.18	0.31	0.18	0.44	0.25	0.07	1.00
G0128	0.42	0.12	0.56	0.00	0.56	0.11	0.00	0.00
G0212	0.66	0.10	0.92	0.06	0.78	0.25	0.01	1.00
G0224	0.43	0.20	0.60	0.16	0.62	0.25	0.00	2.68
M0425	0.55	0.00	0.62	-0.03	0.51	0.25	0.00	1.00
M0520	0.18	0.27	0.18	0.28	0.34	0.48	0.00	0.00
M0523	0.70	0.00	0.73	-0.02	0.57	0.24	0.00	0.00
O1201	0.28	0.19	0.57	0.05	0.52	0.33	0.00	1.00
O1212	0.31	0.16	0.32	0.17	0.49	0.25	0.01	2.73
O1218	0.13	0.38	0.25	0.29	0.70	0.25	0.00	3.72
T_4	0.59	0.00	0.66	-0.02	0.52	0.28	0.00	0.00
T_3	0.30	0.17	0.36	0.12	0.45	0.25	0.04	1.00
T_2	0.26	0.25	0.41	0.17	0.39	0.25	0.10	1.00
T_1	0.48	0.12	0.89	-0.03	0.42	0.25	0.06	1.10

Table 3.3
Regression values of empirical relationships through different data subsets

	ρ (DWR)	ρ (Z_{Ku})	ρ (Z_{Ka})	N
all	0.77	0.52	0.19	1442
GCPEX	0.73	0.73	0.54	461
MC3E	0.62	0.37	0.26	595
OLYMPEX	0.68	0.64	0.53	386
G0128	0.67	0.40	0.05	88
G0212	0.60	0.36	0.13	93
G0224	0.56	0.60	0.39	280
M0425	0.54	0.00	-0.09	191
M0520	0.83	0.91	0.87	211
M0523	0.42	-0.09	-0.17	193
O1201	0.72	0.48	0.12	108
O1212	0.59	0.59	0.54	260
O1218	0.67	0.94	0.47	18
T_4	0.50	-0.03	-0.18	174
T_3	0.64	0.62	0.52	309
T_2	0.70	0.68	0.36	391
T_1	0.69	0.25	-0.13	547

Table 3.4
Correlation Coefficients and Number of measurements in different data subsets

	D_m min (mm)	D_m max (mm)	DWR min (mm)	DWR max (dB)	Z_{Ku} min (dBZ)	Z_{Ku} max (dBZ)	Z_{Ka} min (dBZ)	Z_{Ka} max (dBZ)	T min (°C)	T max (°C)
all	0.2	1.9	-0.2	10.6	3.3	33.2	0.6	28.7	-43	-3
GCPEX	0.3	1.9	-0.2	10.6	7.1	30.2	5.7	24.2	-23	-4
MC3E	0.2	1.2	-0.2	6.7	3.3	33.2	0.6	28.7	-43	-5
OLYMPEX	0.3	1.4	0.3	9.0	6.0	30.4	6.2	27.6	-23	-3
G0128	0.3	0.9	-0.2	3.8	7.1	15.9	6.2	12.8	-23	-4
G0212	0.4	1.7	-0.2	8.3	10.6	30.2	7.2	24.2	-18	-11
G0224	0.3	1.9	0.5	10.6	8.3	28.4	5.7	19.8	-18	-4
M0425	0.3	0.9	0.1	6.7	5.5	24.8	6.3	24.2	-35	-18
M0520	0.2	0.8	-0.2	3.6	5.8	20.0	6.4	19.6	-23	-5
M0523	0.4	1.2	0.9	5.7	3.3	33.2	0.6	28.7	-43	-22
O1201	0.5	1.1	0.7	9.0	15.9	28.8	15.5	23.0	-6	-3
O1212	0.3	1.4	0.3	4.8	6.0	30.4	6.2	27.6	-23	-4
O1218	0.4	1.4	1.7	6.4	16.1	27.1	13.0	23.2	-8	-5
T_4	0.3	1.1	0.2	5.7	5.5	33.2	5.4	28.7	-40	-30
T_3	0.2	1.2	-0.2	6.7	5.8	24.8	6.2	24.2	-30	-20
T_2	0.3	1.7	-0.2	10.3	7.0	30.2	6.7	24.2	-20	-10
T_1	0.3	1.9	0.7	10.6	7.6	30.4	5.7	27.6	-10	-3

Table 3.5
Ranges of radar measurements and in-situ properties for different data subsets

The scattered Z_{Ku} and D_m data are first grouped differently in different experiments (Figure 3.8). The Z_{Ku} and D_m data from GCPEX form a visibly-correlated linear relationship that is similar in form to the GCPEX DWR-D_m relationships. The Z_{Ku} and D_m data from MC3E displays no visible correlation. The Z_{Ku} and D_m from OLYMPEX form a curved wedge. Z_{Ku} is associated with a mostly constant Dm value for $Z_{Ku} < 17$ dBZ, but as Z_{Ku} increases, the maximum D_m increases while the minimum D_m remains mostly unchanged. The scattered DWR and D_m data for different experiments all have the same grouping as the combined dataset in Figure 3.7c, but extended out to different maximum DWR values.

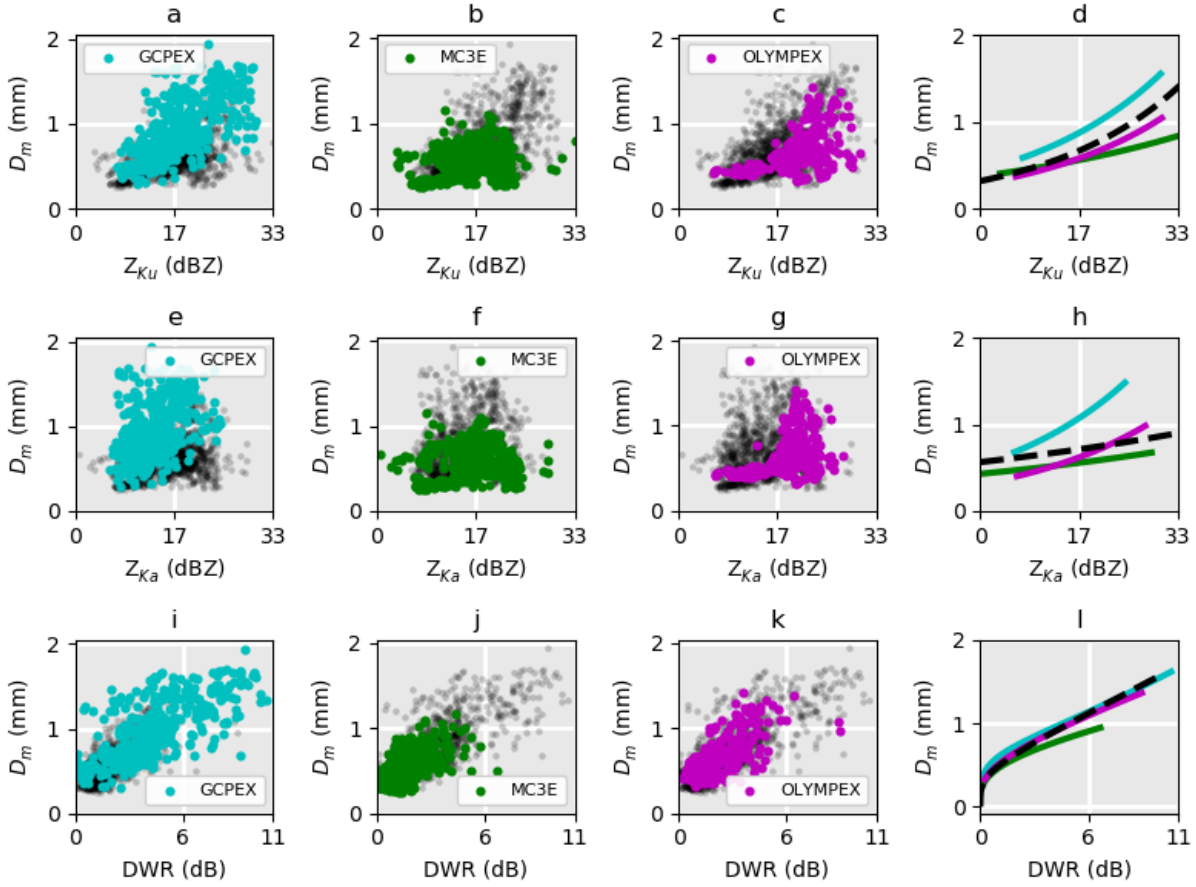

Figure 3.8
As in Figure 3.7, but data is separated with respect to different experiments. Empirical regressions from different experiments are presented for Z_{Ku} (d), Z_{Ka} (h), and DWR (l), respectively.

The empirical relationships between Z_{Ku} and D_m from different experiments all deviate from the Z_{Ku}-D_m relationships in Figure 3.7a. GCPEX data always retrieves higher D_m than the empirical relationships drawn from MC3E, OLYMPEX, or the combined dataset. The GCPEX and OLYMPEX Z_{Ku}-D_m relationships have similar curvature, while the poorly correlated MC3E Z_{Ku}-D_m relationship has a flatter slope. Because of this, Z_{Ku}-D_m empirical relationships for MC3E and OLYMPEX are similar for $Z_{Ku} < 17$ dBZ, but OLYMPEX retrieves larger D_m as Z_{Ku} increases beyond 17 dBZ. the Z_{Ka} and D_m results are similar to Z_{Ku} and D_m results, such that the empirical relationships appear more correlated during GCPEX and OLYMPEX.

The empirical relationships between DWR and D_m for individual experiments all begin similarly. MC3E and OLYMPEX relationships peel off from the combined relationship towards lower D_m at the highest DWR provided by the respective experiments. In both cases this deviation mostly occurs in regions where data appears to be represented by sparse and high influence outliers. GCPEX data is similar to the combined relationship across the entire range of D_m, though it predicts slightly higher D_m for DWR < 5 dB.

Z_{Ku} and D_m also have different ranges and grouping during different IOPs (Figure 3.9), though in several cases, the grouping and relationships between different IOPs appear similar. The three OLYMPEX IOPs each had different ranges of Z_{Ku}, but the empirical relationships from O1201 and O1212 are almost identical, and they overlap with the empirical relationship from O1218. Z_{Ku} and D_m data had similar ranges of data and grouping during G0212 and G0224. During G0128, Z_{Ku} and D_m were much lower, so the empirical relationships do not overlap well with the other two IOPs, but the G0128 scattered data still lies in a similar regime as the low reflectivity data from G0224. MC3E IOPs had similar ranges of D_m between IOPs, and Z_{ku} and D_m are both uncorrelated during M0425 ($\rho = 0$) and M0523 ($\rho = -0.09$), but they are highly correlated during M0520 ($\rho = 0.87$). Scattered Z_{Ka} and D_m data have similar grouping as Z_{Ku} and D_m, but Z_{ka} and D_m are only visibly correlated during M0520 and O1212 for $Z_{Ka} < 12$ dBZ (Figure 3.10).

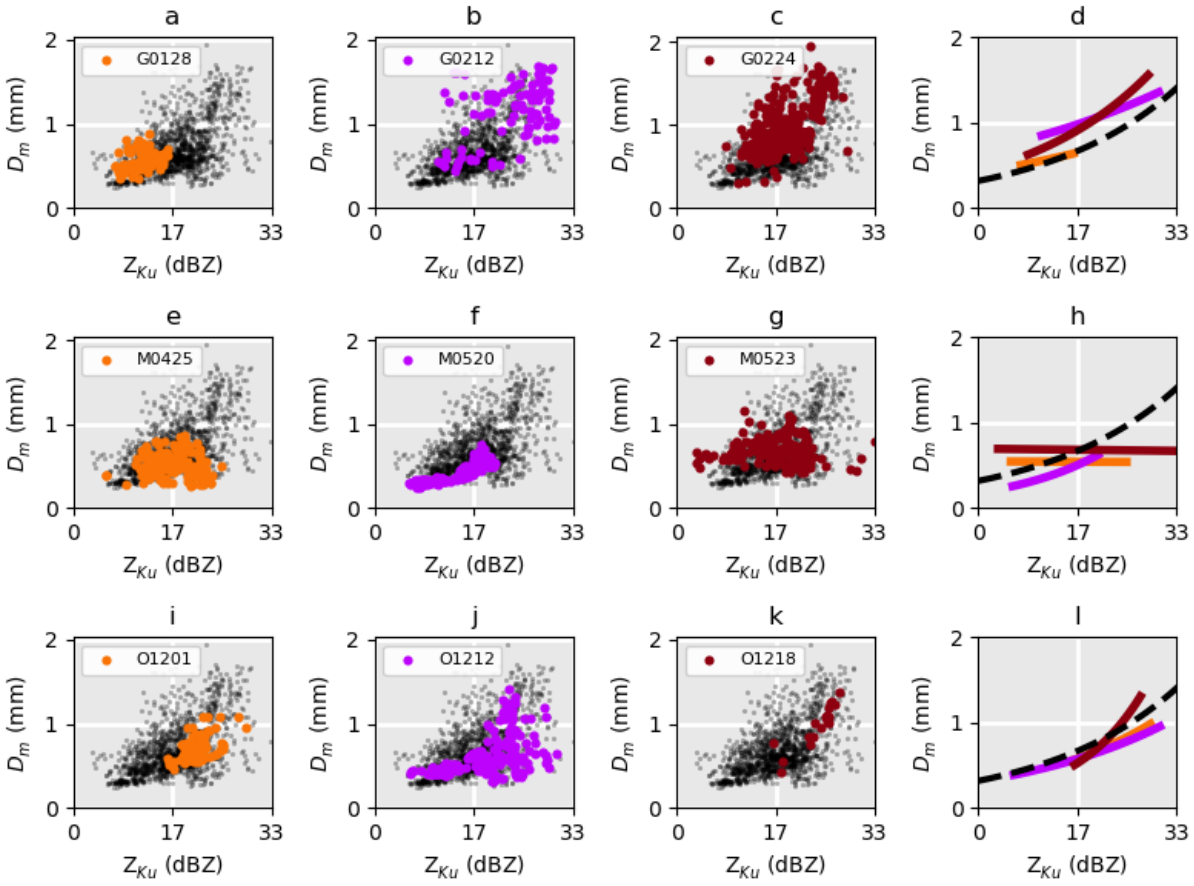

Figure 3.9
As in Figure 3.7, but just for Z_{Ku}, and data are separated into different IOPs. Empirical regressions are presented for GCPEX (d) , MC3E (h) , and OLYMPEX (l) IOPs.

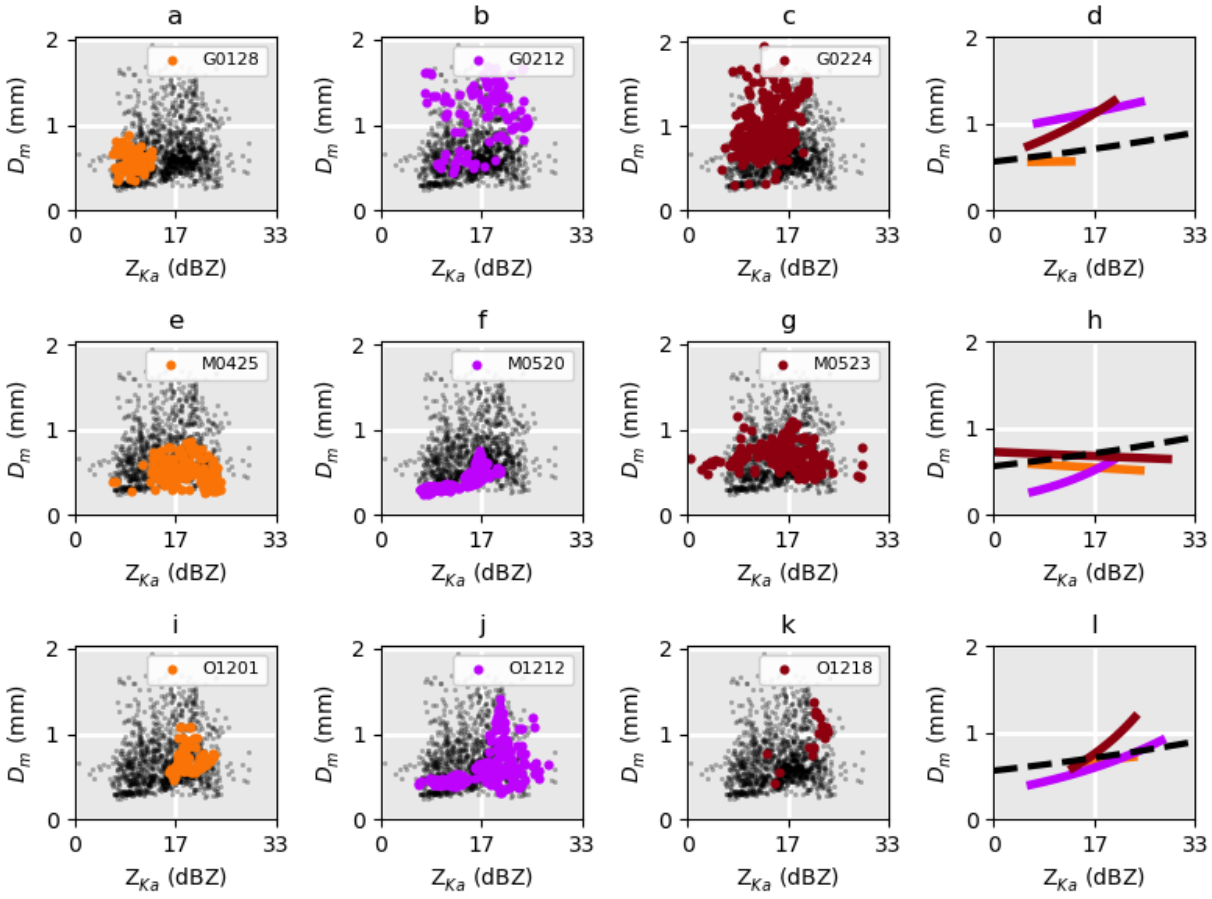

Figure 3.10
As in Figure 3.9, but for Z_{ka}.

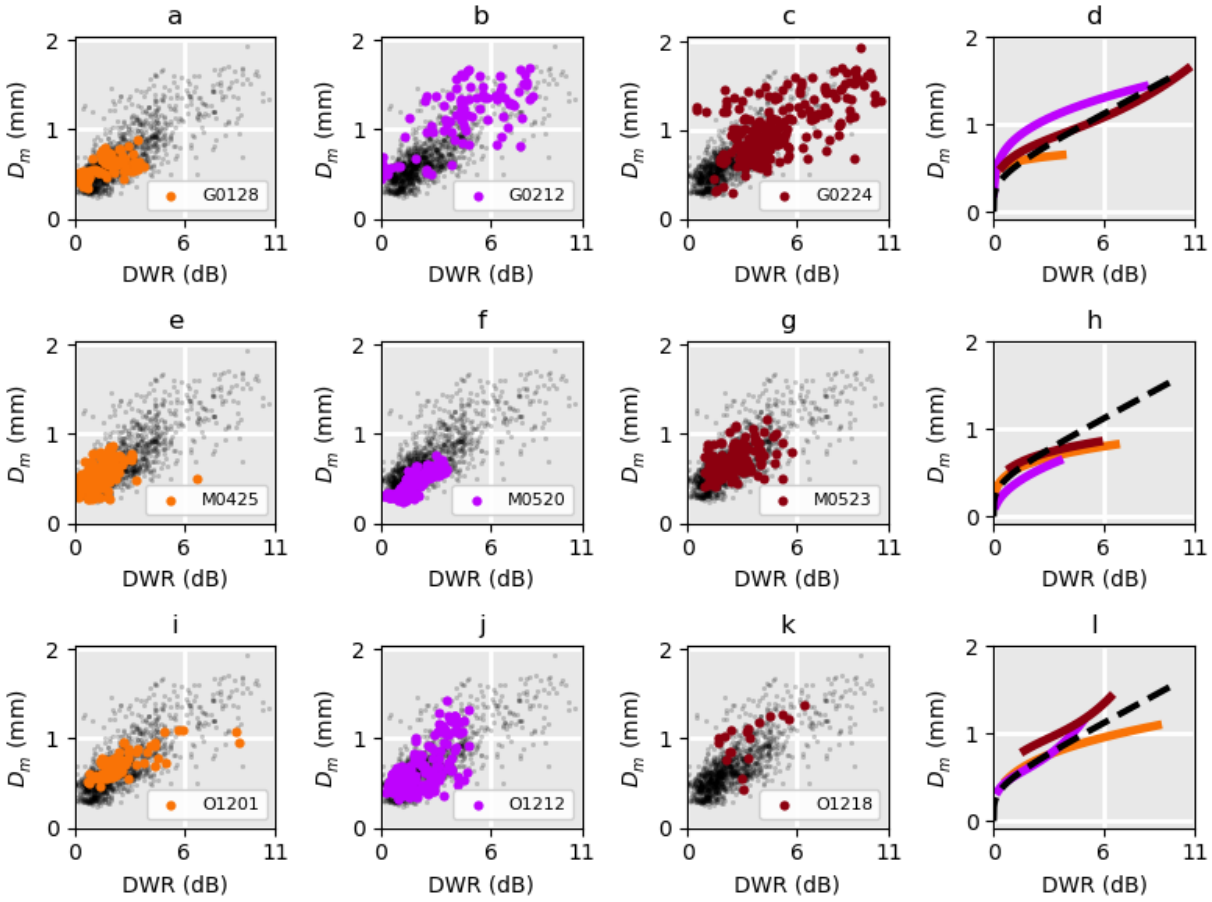

Figure 3.11
As in Figure 3.9, but for DWR.

DWR and D_m from different IOPs have mostly similar grouping, even if they come from different experiments (Figure 3.11). G0128, M0425, M0520, M0523, and O1201 all provide data that is mostly described by a linear relationship with DWR < 6 dB and D_m < 1 mm, and aside from some systematic tendencies for higher and lower D_m during M0425 and M0520 that don't greatly impact the empirical relationships, the IOPs all describe a similar relationship. G0212, G0224, and O1212 are the only IOPs that provide large amounts of D_m > 1 mm. G0212 and G0224 have a notably loose grouping relative to other IOPs, with D_m > 1 mm corresponding to the entire range of witnessed DWR. D_m > 1 mm during O1212, by contrast, is limited between 3 and 5 dB. The looser grouping during GCPEX IOPs is likely because the high DWR observations came from thin cloud features with sharp DWR and D_m gradients, where individual measurements sometimes changed by a full dB or mm from one measurement to the next (Figure

5). Minor time lags between collocated radar and *in-situ* measurements or differences in average PSDs of changing environments between different sample volumes could both decrease correlation during those IOPs. The G0212 DWR-D_m empirical relationship has negative and linear curvature across its entire span. The G0224 DWR-D_m empirical relationship has a negative and linear curvature until DWR exceeds 8 dB, whereupon it begins to curve upward slightly. The O1212 DWR-D_m empirical relationship begins to gain a positive curvature as DWR exceeds 3 dB.

Data are finally separated into four subsets based on temperature in Figure 3.12. These groups are referred to as T_4 ($-40 < T < -30$), T_3 ($-30 < T < -20$), T_2 ($-20 < T < -10$), and T_1 ($-10 < T < 0$). The differences between temperature-dependent empirical relationships are mostly related to a maximum D_m of 1 mm that only exists for temperatures below -20°C. Otherwise, the grouping of radar measurements and D_m fill out the same shape as those from Figure 3.7. The Z_{Ku} and D_m subsets have different correlations, so the corresponding empirical relationships have different slopes. The Z_{Ka} and D_m subsets are all very poorly correlated, and half of the relationships imply decreasing Z_{Ka} with increasing D_m. The DWR-D_m empirical relationships have similar shapes, but slightly different curvatures that lead to consistent differences in retrieved D_m. T_2 retrieves the highest D_m for a given DWR, T_1 retrieves slightly lower D_m, followed by T_3, and then T_4.

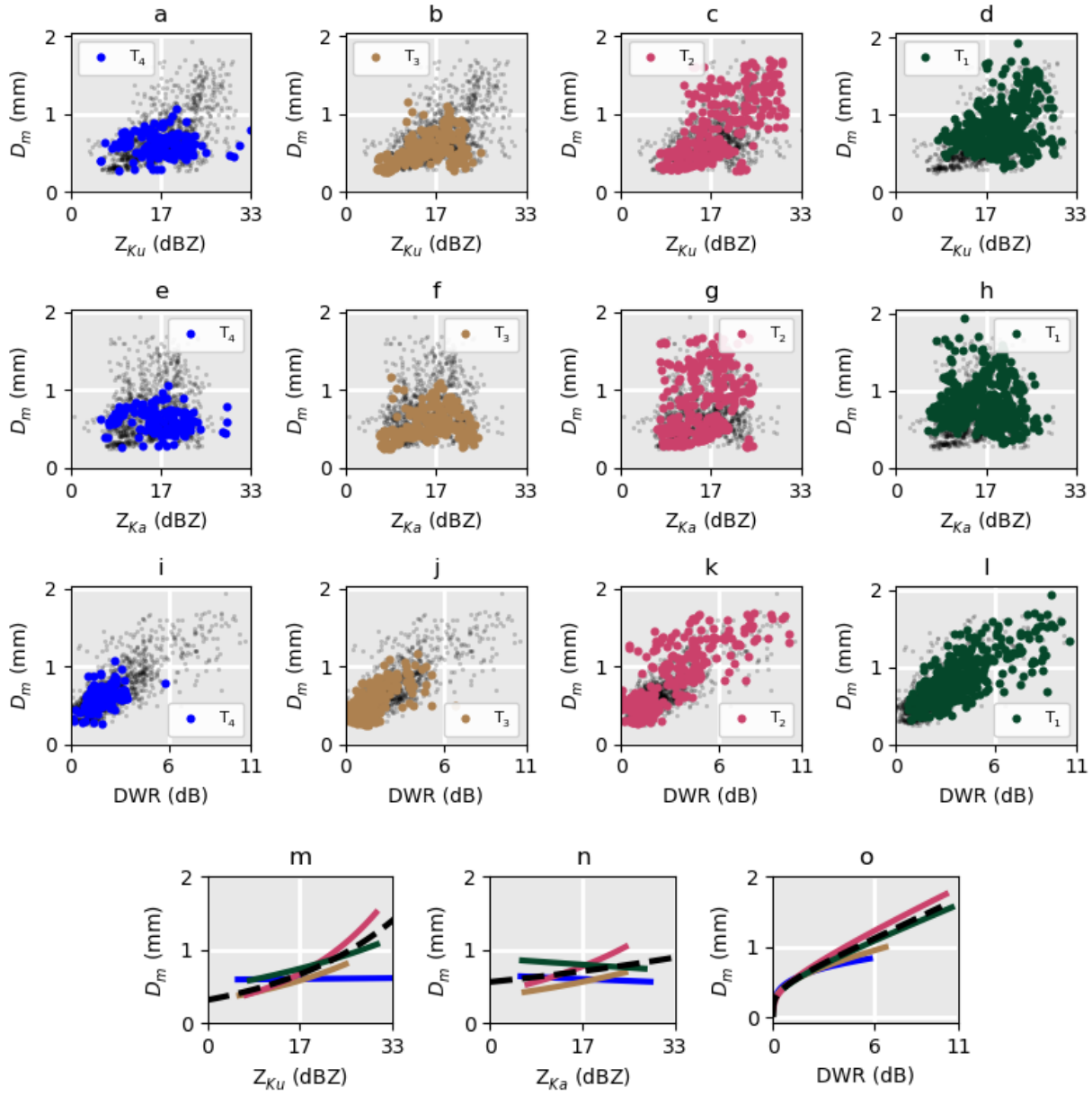

Figure 3.12
As in Figure 3.7, but for different temperature ranges. Empirical regressions from different temperature ranges are presented in Figures 10m, 10n, and 10o for Z_{Ku}, Z_{Ka}, and DWR, respectively.

There was at least one intersection where D_m *only* appeared to be related to DWR (Figure 3.13). During O1212 at 19.5 h, D_m decreased from 6 mm down below 3 mm at 19.52 h, rising back up to 5 mm at 19.56 h. During this same time period, DWR began at 5dB, dropped to 3dB at 19.52 hr, and rose to 4 dB at 19.56. Z_{Ku} remained around 22.5 dBZ during this whole time period, even

though reflectivity is known to be influenced by particle sizes. It is beyond the scope of this study to investigate why Z_{Ku} wasn't correlating with D_m as would be expected, but this intersection provides a clear and simple example where DWR provided unique information on D_m that couldn't be gathered from a single wavelength radar.

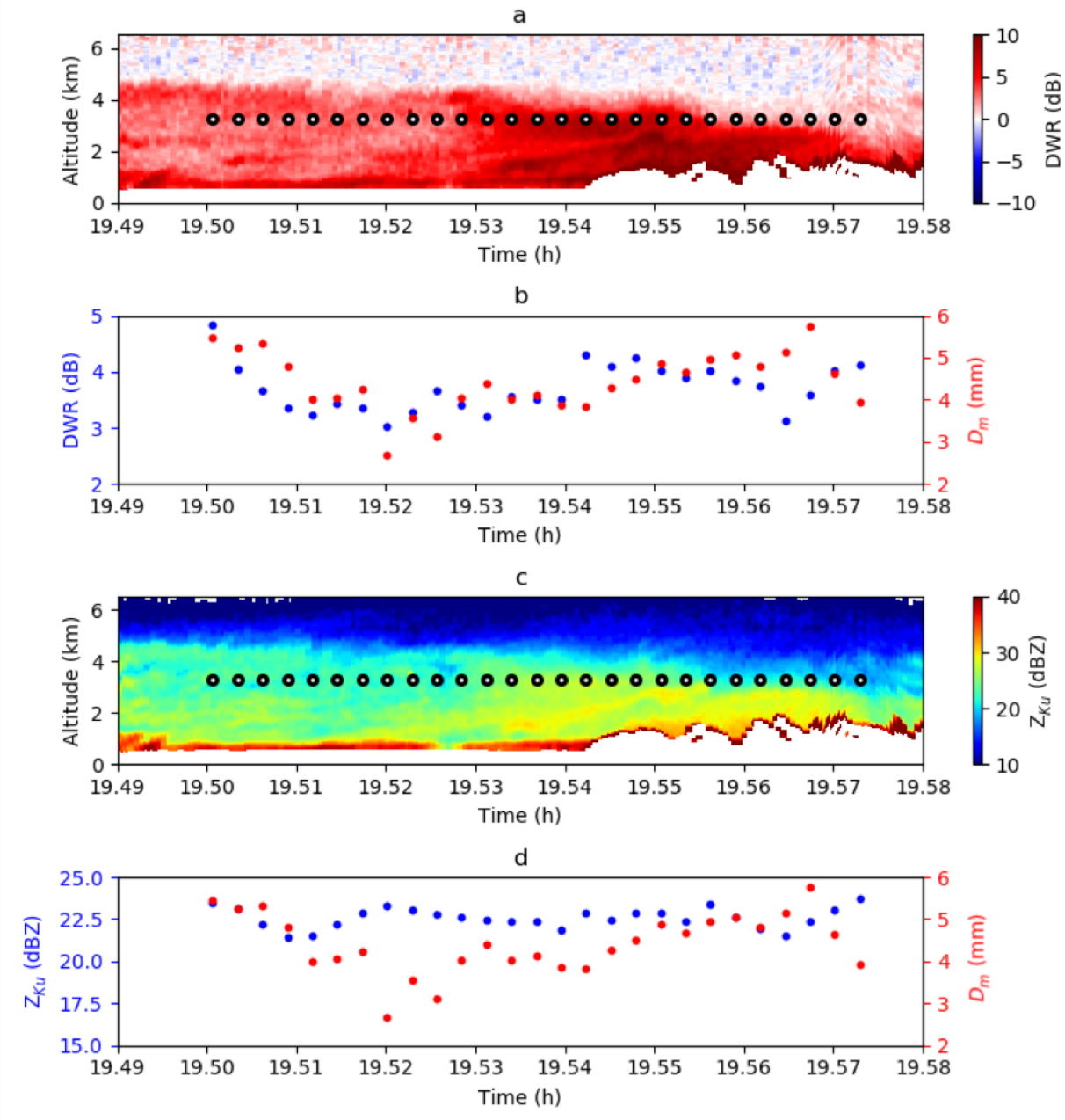

Figure 3.13
A sample of collocated data during O1212, displaying collocated DWR profiles and Citation altitude (a), collocated DWR and D_m (b), collocated Z_{Ku} profiles and Citation altitude (c), and collocated Z_{Ku} and D_m (d).

3.4.3 RETRIEVAL EVALUATIONS

The third set of results addresses the question: "Does a DWR-based D_m retrieval method provide more accurate and consistent results than a Z-based D_m retrieval method?" Three retrieval methods are considered: the empirical relationship through the combined dataset (C), a set of empirical relationships for each experiment (E), and a set of empirical relationships for the four temperature regimes (T). These relationships were derived in Section 3.4.2. Empirical relationships are considered for DWR, Z_{Ku}, and Z_{Ka}, resulting in nine retrieval methods. The D_m retrieved from the combined data set through these nine methods (D_m ret.) are compared with the measured D_m (D_m meas.) in Figure 3.14. RMSE and bias for the nine methods across the data subsets defined in Section 3.4.2 are presented in Table 3.6 and Table 3.7.

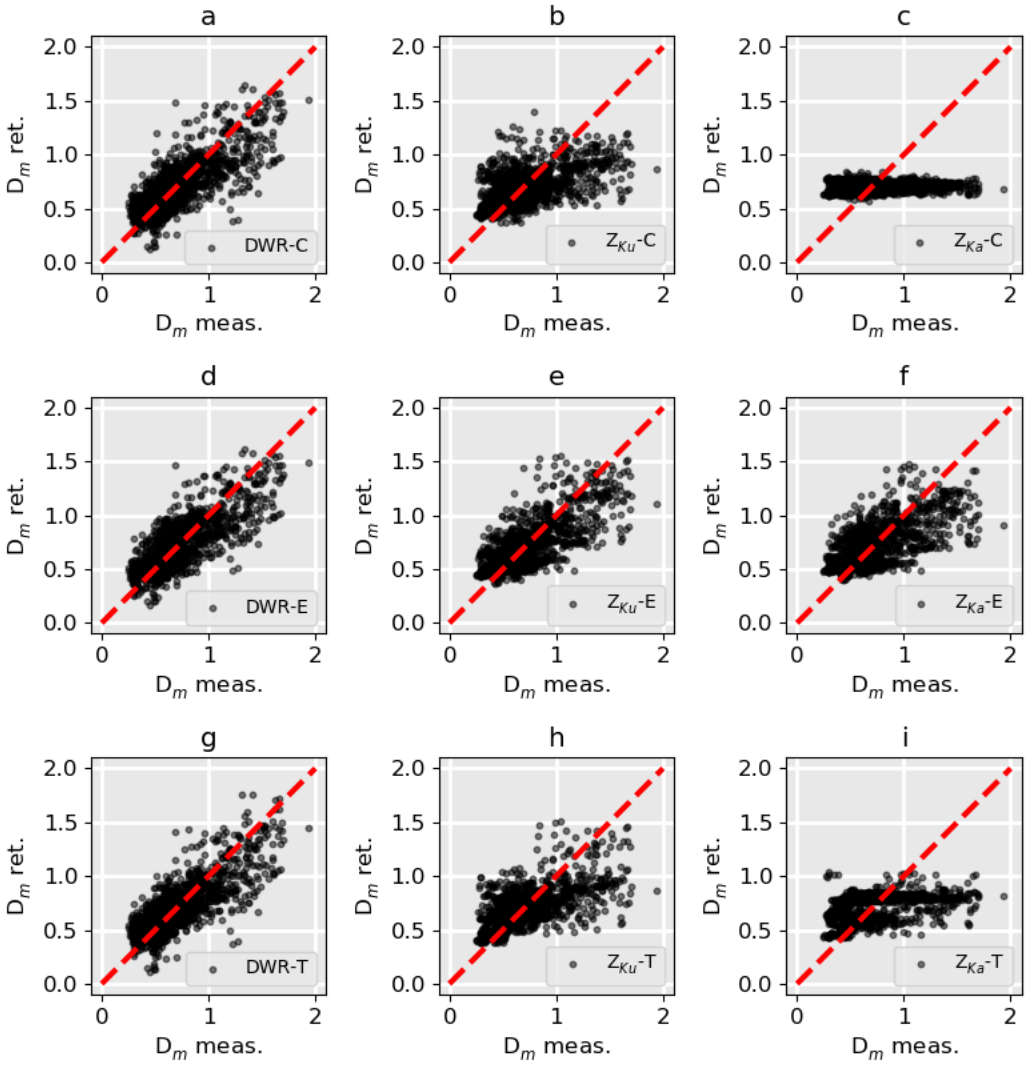

Figure 3.14
Evaluations of D_m retrieved through different empirical retrieval methods (Dm ret.) against Dm measured by the Citation.

Retrieval Bias (mm)

	DWR-C	Z_{Ku}-C	Z_{Ka}-C
GCPEX	-0.06	-0.22	-0.26
MC3E	0.05	0.10	0.15
OLYMPEX	-0.02	0.10	0.07
G0128	-0.02	-0.04	0.08
G0212	-0.22	-0.25	-0.44
G0224	-0.02	-0.26	-0.31
M0425	0	0.13	0.18
M0520	0.15	0.16	0.25
M0523	-0.01	0.00	0.02
O1201	0	0.11	0.04
O1212	-0.01	0.11	0.10
O1218	-0.19	-0.07	-0.24
T4	0.01	0.08	0.11
T3	0.01	0.07	0.16
T2	-0.04	-0.03	-0.04
T1	0.02	-0.04	-0.10

Table 3.6
Bias of between D_m ret. and D_m meas. for different data subsets from DWR-C, Z_{ku}-C, and Z_{Ka}-C retrieval methods**.** Bolded numbers represent the minimum bias for a data subset

Retrieval RMSE (mm)

	DWR-C	DWR-E	DWR-T	Z_{Ku}-C	Z_{Ku}-E	Z_{Ku}-T	Z_{Ka}-C	Z_{Ka}-E	Z_{Ka}-T
All Data	0.19	0.18	0.18	0.25	0.20	0.24	0.30	0.22	0.28
GCPEX	0.25	0.24	0.24	0.34	0.25	0.31	0.42	0.30	0.37
MC3E	0.15	0.14	0.15	0.20	0.16	0.18	0.23	0.17	0.22
OLYMPEX	0.16	0.16	0.16	0.21	0.18	0.21	0.22	0.20	0.21
G0128	0.14	0.16	0.14	0.12	0.18	0.09	0.14	0.26	0.17
G0212	0.33	0.30	0.30	0.41	0.34	0.38	0.55	0.37	0.50
G0224	0.24	0.24	0.24	0.36	0.24	0.33	0.42	0.28	0.36
M0425	0.13	0.13	0.13	0.21	0.15	0.19	0.23	0.14	0.20
M0520	0.17	0.13	0.17	0.17	0.12	0.18	0.27	0.14	0.27
M0523	0.14	0.15	0.14	0.22	0.20	0.17	0.16	0.21	0.19
O1201	0.10	0.09	0.10	0.16	0.11	0.18	0.14	0.14	0.17
O1212	0.17	0.17	0.17	0.23	0.20	0.23	0.24	0.21	0.22
O1218	0.28	0.27	0.29	0.16	0.26	0.20	0.33	0.32	0.33
T4	0.12	0.12	0.11	0.21	0.15	0.13	0.18	0.15	0.13
T3	0.14	0.14	0.13	0.17	0.16	0.15	0.23	0.17	0.17
T2	0.24	0.22	0.24	0.30	0.23	0.28	0.38	0.26	0.37
T1	0.19	0.19	0.19	0.28	0.21	0.27	0.30	0.24	0.28

Table 3.7
RMSE between Dm meas. and Dm ret. for different data subsets from all retrieval methods. Bolded numbers refer to the minimum RMSE for a data subset, ignoring the italicized results from DWR-E and DWR-T methods.

The range of D_m ret. changes with different retrieval methods. Broader ranges of D_m ret. that match the measured range of D_m appear to have the best agreement with measured data, and they are distributed more evenly about the 1:1 line. Retrieval methods that provide smaller ranges of D_m ret. provide disproportionately large underestimates of Dm ret. Dm ret. spans the full length of measured D_m for all DWR-based retrievals, and there is little improvement associated with more sensitive retrieval methods. The range of Dm ret. is mostly between 0.4 and 1.25 mm for the Z_{Ku}-C method, but this range increases as more sensitive retrieval methods are used. The Z_{Ka}-C retrieval method has the smallest range of D_m ret., just between 0.6 and 0.9.

In all but one data subset, the combined DWR-D_m empirical relationship either provides the lowest bias, or it agrees with the method that provides the lowest bias within 0.01 mm. The D_m ret. from the DWR-C retrieval method are biased less than 0.02 mm across most data subsets. The Dm ret. from Z-C retrieval methods regularly exceed 0.1 mm.

The DWR-C retrieval also tends to provide lower RMSE across the combined data set and across all data subsets than any Z-based retrieval, including the environmentally-dependent retrieval methods. The environmentally dependent retrieval methods tend to reduce the RMSE from the Z-based retrievals, but across most data subsets, they only provide a 0.01 mm improvement in RMSE for the DWR-based retrieval. Z_{Ka} retrieval methods had a substantial increase in retrieval accuracy when experiment-specific relationships were used. The Z_{Ka}-E RMSE is greater than the Z_{Ku}-E RMSE for the combined dataset, but it is less than the Z_{Ka}-T RMSE.

3.5 DISCUSSION AND CONCLUSION

GPM's DPR can conduct novel DWR-based retrievals of D_m. This DWR-based method is believed to be superior to a single wavelength Z-based method, but to our knowledge, the capabilities of the two methods had not been compared against each other with measured data. In this study, empirically generated Z and DWR-based retrievals of D_m were evaluated in diverse snow clouds. Data came from three experiments, GCPEX, OLYMPEX, and MC3E, which represented winter synoptic and lake-effect storms near Ontario, winter orographic, and synoptic storms near the Olympic Mountains, and late-spring convective storms in Oklahoma. Collocated

data and empirical relationships were presented for the combined data set, for subsets of individual experiments, IOPs, and temperature ranges.

The relationships between DWR and D_m across all experiments, IOPs, and temperature ranges in this study were adequately described with a common relationship defined by Equation 5, with $c_3 = 0.43$, $c_4 = 0.25$, $c_5 = 0.06$, and $c_6 = 1.17$. The relationships between Z_{Ku} and D_m were inconsistent between different environments. In IOPs that had similar ranges of DWR, such as G0128, O1201, and M0425, Z_{Ku} had completely different ranges across the full span of observed reflectivity. The relationships between Z_{Ku} and D_m were uncorrelated during M0425 and M0523, but they were strongly correlated during M0520.

The DWR-based retrieval demonstrates a decreased RMSE and bias across most data subsets compared to Z-based retrievals, even when Z-based retrievals are allowed to incorporate environmental-specific retrieval methods. The DWR-D_m relationship from the combined data set represents the first empirically based retrieval method of D_m that can be applied to DWR measurements, and it would be straightforward to apply this relationship to global retrievals of D_m from DPR measurements.

The relationship between DWR and D_m is in agreement with theoretical relationships between DWR and D_m (Figure 3.15). It is worth noting that PSDs with $D_m > 1$ mm were mostly provided by two IOPs, namely G0212 and G0224. These IOPs describe a mostly linear relationship for all DWR and D_m that is most similar to the predictions from a spheroidal scattering model. The only non-GCPEX IOP to provide a considerable amount of D_m data was from O1212, and this high D_m data generates the only DWR-D_m relationship from any IOP with a positive curvature below 6 dB (Figure 11l). This relationship is more similar to the predictions from a heterogeneous scattering model. However, D_m in this range of DWR is also found in G0212 and G0224, and there is not a comparably large amount of data from O1212 above 1 mm, so it is not certain whether this grouping truly represents a positively curved DWR-D_m relationship or whether it represents a region of data within the uncertainty of the same DWR-D_m relationship described by the GCPEX data. It would be valuable to repeat this study with more $D_m > 1$ mm to investigate the predicted differences in DWR-D_m relationships from different snowflake habits at large D_m.

The grouping of Z_{Ku} and D_m between different IOPs in Figure 9 revealed an unexpected result: $Z_{Ku} - D_m$ relationships appear to fall into different modes that consistently correspond with different environments: GCPEX clouds, non-GCPEX clouds with temperatures colder than -20°C, and non-GCPEX clouds with temperatures warmer than -20°C. These results are rearranged to demonstrate these common modes in Figure 16. These different cloud types can be more abstractly described in several ways (e.g.: snowing clouds and raining clouds, stratiform clouds and convective clouds), and the -20°C temperature demarcation separates the different cloud regimes where large snowflake aggregation can or cannot occur. However, a full investigation of this matter is beyond the scope of this study. A convincing identification of environmentally distinct and consistent single-wavelength empirical retrieval relationships would be valuable for the satellite radar community, and a dedicated investigation into these proposed regimes with a larger and more diverse collocated Z-D_m dataset is encouraged.

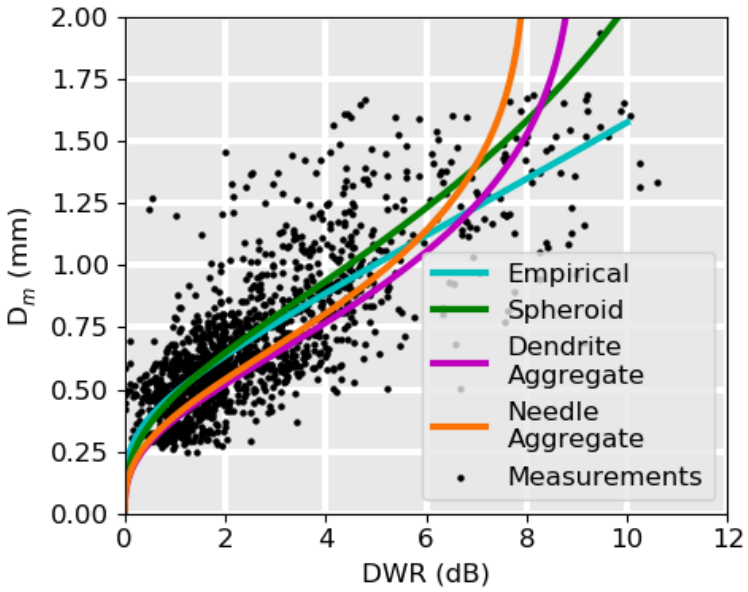

Figure 3.15
The empirical DWR-D_m relationship and collocated data are compared with the theoretical relationships from Figure 3.6.

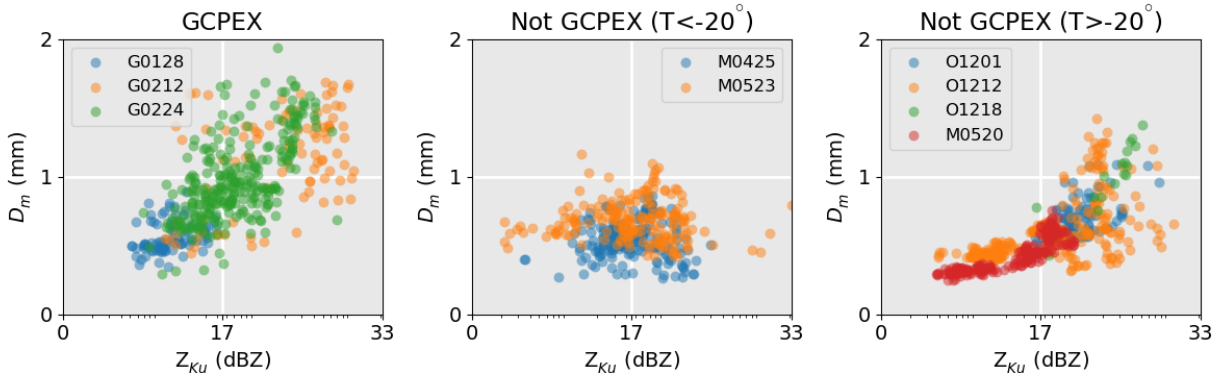

Figure 3.16
A rearrangement of Figure 3.9 to reveal common modes between different IOPs

DWR measurements of precipitation are a unique source of information that GPM can provide. Through the evaluations in this study, we have demonstrated that DWR provides an improved retrieval of D_m compared to Z-based retrievals, and we have demonstrated that ranges of collocated Z and DWR can vary considerably, implying that some microphysical properties which only change the single-wavelength reflectivity of a cloud might be identifiable through a combination of single and dual wavelength reflectivity measurements. More studies involving collocated dual-frequency radar and *in-situ* measurements may continue to reveal valuable information that can only be gathered from the GPM core satellite.

CHAPTER 4 EVALUATIONS OF SNOWFLAKE SCATTERING MODELS AGAINST EXPERIMENTAL MEASUREMENTS

4.1 INTRODUCTION

4.1.1 MOTIVATION

An essential component of NASA precipitation retrievals is the retrieval of D_m from DWR. The snow particle scattering model used to simulate DWR-D_m relationships in the GPM 2A-DPR retrieval product (Seto et al. 2013; hereafter referred to as the GPM algorithm) was not modified significantly modified from the TRMM retrieval algorithm used to retrieve PSDs in tropical storms, however. Several of the assumptions in this algorithm that model snowflakes as spherical particles in clouds with high liquid water content run against the consensus from *in-situ* observations of midlatitude snowing clouds (Leinonen et al. 2018; Chase et al. 2018; Yin et al. 2017; Kneifel et al. 2015; Petty and Huang 2010; Hogan et al. 2012). Since there has not yet been an evaluation of the GPM algorithm against measured data, however, it has not been known whether these assumptions amount to any problematic biases in retrieved data. In fact, without the measured relationship between DWR and D_m provided in this dissertation, there has not yet been a direct evaluation of the DWR-D_m relationship predicated by any of the models that portray snowflake scattering processes with different shape assumptions.

4.1.2 RESEARCH STATEMENT AND METHOD

The matched DWR and D_m data generated in the previous chapter provides a novel method to evaluate assumptions in retrieval algorithms. Each scattering model is linked to a unique simulated DWR-D_m relationship, and the empirical relationship provides the best current estimate of the relationship between DWR and D_m in real snow clouds. Therefore, simulated DWR-D_m relationships that deviate from the empirical relationship are likely to indicate a poor representation of the snow particles within typical snowing clouds. In this chapter, I conduct the

first comparisons between theoretical and measured DWR-D_m relationships. The theoretical relationships are introduced in Section 4.2, evaluations are conducted in Section 4.3, and the study is summarized in Section 4.4.

4.2 THEORY

4.2.1 MODEL ASSUMPTIONS

Model PSDs are calculated following Equation 3-8. DWR is simulated by applying PyTmatrix (Leinonen 2014)spheroidal cross-sections to Equation 3-1 and Equation 3-7. Spheroids are initially calculated with sizes of D_{meas}, so they can use the same mass parameterizations as imaged particles (e.g., Heymsfield et al. 2010). Spheroids can take the form of "oblate spheroids," with two major axes and one minor axis, or "prolate spheroids," with two minor axes and one major axis. Oblate or prolate spheroids are generated in PyTmatrix with AR greater-than or less-than one, respectively. AR is referred to alongside an abbreviation of (Ob) or (Pr), referring to oblate or prolate spheroids, respectively. ODFs are described by Gaussian probability distribution functions with assumed 0° average orientations representing "fluttering" snowflakes (G-σ, with σ representing the standard deviation), delta functions centered on 0° representing horizontally oriented snowflakes (HO), or uniform probability distribution functions representing randomly oriented snowflakes (RO).

As previously mentioned, the GPM algorithm assumes a spherical particle with a constant density (implying a *b* of 3). If a radar bright band (BB) is detected, referring to the layer of melting snow that has a visibly higher reflectivity than the clouds above or below it, the GPM algorithm has a temperature-dependent set of DWR-D_m relationships. If no bright band is detected (noBB), just a single DWR-D_m relationship is used. The justification for these assumptions is unclear. A *b* of 3 for is a valid assumption for graupel particles, but in stratiform clouds where large dendritic snowflakes will often dominate the measured PSDs, *b* has consistently been derived as closer to 2 (Heymsfield et al. 2010; Brown and Francis 1995; Locatelli and Hobbs 1974). There is also little physical difference between a cloud of frozen

precipitation that continues to the ground as snowfall versus a cloud of frozen precipitation that melts closer to the surface, so the rationale behind the conditionally temperature-dependent DWR-D_m is also unclear. On the contrary Figure 3.7 displayed a remarkably similar DWR-D_m relationship among data drawn from noBB clouds (GCPEX) and BBclouds (MC3E, OLYMPEX).

The GPM DWR-D_m relationships are difficult to recreate numerically or analytically, so they are iimplied through collocated DWR and D_m data drawn from 100 random 2A-DPR single-orbit data sets. Z_{Ku} (Z_{Ka}) reflectivity comes from the NS (MS) – SLV -zFactorCorrected groups of 2A-DPR files. D_m comes from the NS-SLV-paramDSD group of the same files.

4.2.2 SIMULATED RELATIONSHIPS

Given the lack of commonly accepted recommendations for snow particle microphysical properties, many different parameterizations are similarly plausible. Figure 4.1 demonstrates the sensitivity of spheroid-based simulated relationships to different combinations of literature-recommended snow particle parameterizations (Leinonen et al. 2012; Heymsfield et al. 2010; Hogan et al. 2012; Brown and Francis 1995; Seto et al. 2013; Liao et al. 2016; Mason et al. 2018; Jiang et al. 2019). The parameterizations corresponding to each curve are provided in Table 4.1.

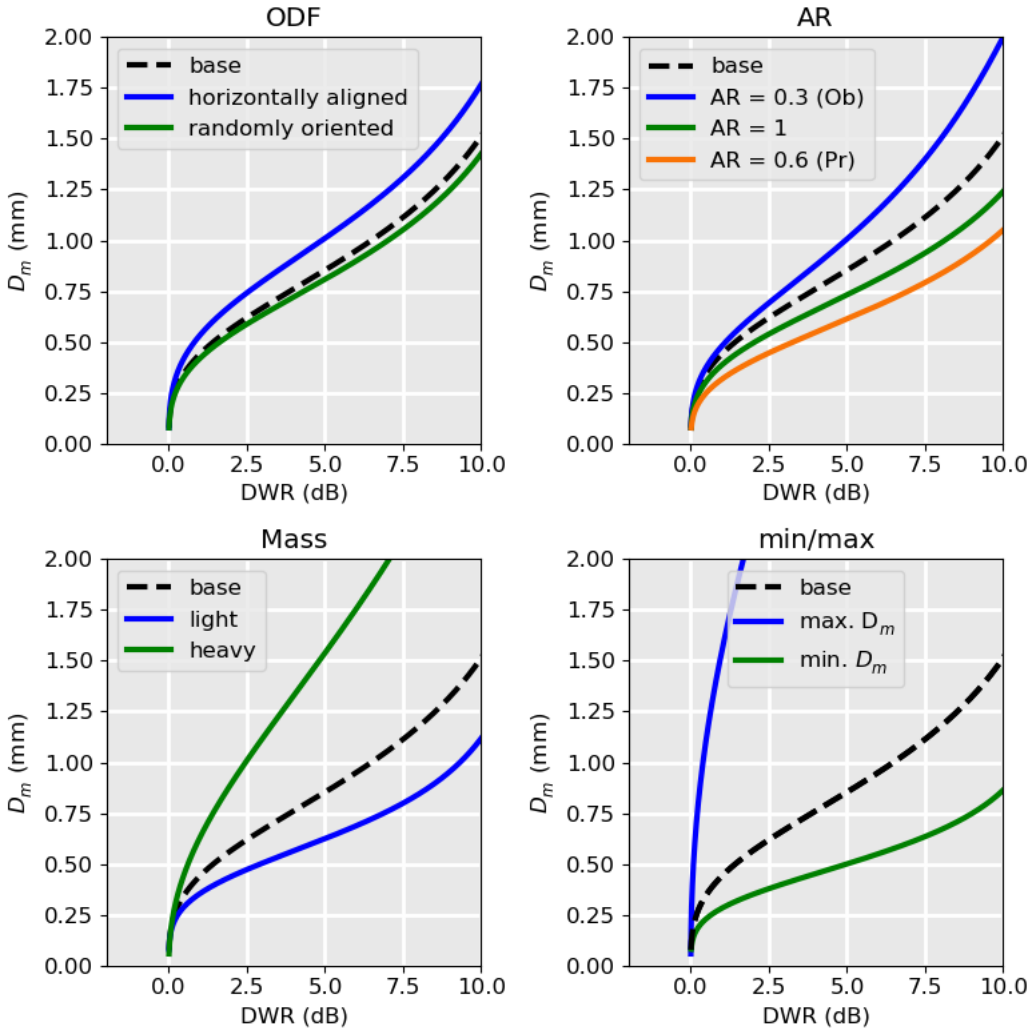

Figure 4.1
Sensitivity tests for simulated DWR-Dm relationships resulting from variations in the ODF (left), AR (middle), and mass (right) parameterizations for spheroid scattering models.

	a (g cm^{-b})	b	AR	ODF
Base	0.007	2.2	0.6 (Ob)	G-40
ODF = HO	0.007	2.2	0.6 (Ob)	HO
ODF = RO	0.007	2.2	0.6 (Ob)	RO
AR = 0.3 (Ob)	0.007	2.2	0.6 (Ob)	G-40
AR = 1	0.007	2.2	1	N/A
AR = 0.6 (Pr)	0.007	2.2	0.6 (Pr)	G-40
Light	0.002	1.9	0.6 (Ob)	G-40
Heavy	0.1	3	0.6 (Ob)	G-40
Max Dm	0.1	3	0.3 (Ob)	HO
Min Dm	0.002	1.9	0.6 (Pr)	RO

Table 4.1
Parameterizations for the simulated DWR-Dm relationships in Figure 4.1

DWR-D_m relationships parameterized with a narrower ODF, a heavier mass parameterization, and higher AR for oblate spheroids will all increase retrieved D_m. AR is peculiar in that the retrieved D_m will deviate from a spherically-generated relationship in opposite directions with decreasing AR depending on whether the spheroids are prolate (decreasing D_m) or oblate (increasing D_m). Interactions between parameters can introduce less-visible sensitivities. For example, there is a noted sensitivity to changes in ODF from the base relationship, but since symmetry forbids this sensitivity for spheres, it can be inferred that the sensitivity from ODF is dependent on AR. Also, while changes in AR and ODF only affect simulated DWR, changes in *a* and *b* will also impact calculations of D_m. Therefore, the "D_m" of simulated DWR-D_m relationships with different mass will represent different moments of a modeled size distribution. Finally, AR changes the geometric scattering properties of snow particles, but it also changes the density through changes in spheroid volume. Therefore, changes in AR are inherently linked to changes in mass parameterizations, and prolate particles will be more sensitive to changes in *a* and *b* than oblate particles. When the interacting sensitivities of the DWR-D_m relationship are optimized, it results in the incomparable maximum and minimum DWR-D_m relationships of Figure 4.1d. It is important to emphasize here that, while the parameterizations in Figure 4.1d are

drawn independently from literature sources, they have never explicitly been recommended in combination.

The BB and noBB GPM DWR-D_m relationships are visualized in Figure 4.2 and colored by temperature. As previously mentioned, the DWR-D_m relationship is temperature independent in clouds with no BB, but it is temperature-dependent in clouds with a BB. The two relationships are identical at very cold temperatures, but they differ substantially at warmer temperatures. The temperature-dependent noBB relationship leads to some unrealistic implications. If one imagines a snow cloud carrying some constant DWR located in a cloud at -5°C, according to the GPM algorithm, this cloud can have a D_m that changes by a mm, sometimes doubling in size, depending on whether it is snowing or raining at the surface. Such a difference in precipitation phase can come from just a few degrees change in surface temperature or even a change in elevation within the same storm, so there is no physical basis for such a distinction. The noBB DWR-D_m relationship also predicts that a negative DWR can correspond to over half of the retrievable range of D_m at warm temperatures. For frozen particles, Ku reflectivity should always be larger than Ka reflectivity, and Ka attenuation will always be larger than Ku attenuation, so a negative DWR should not be permissible.

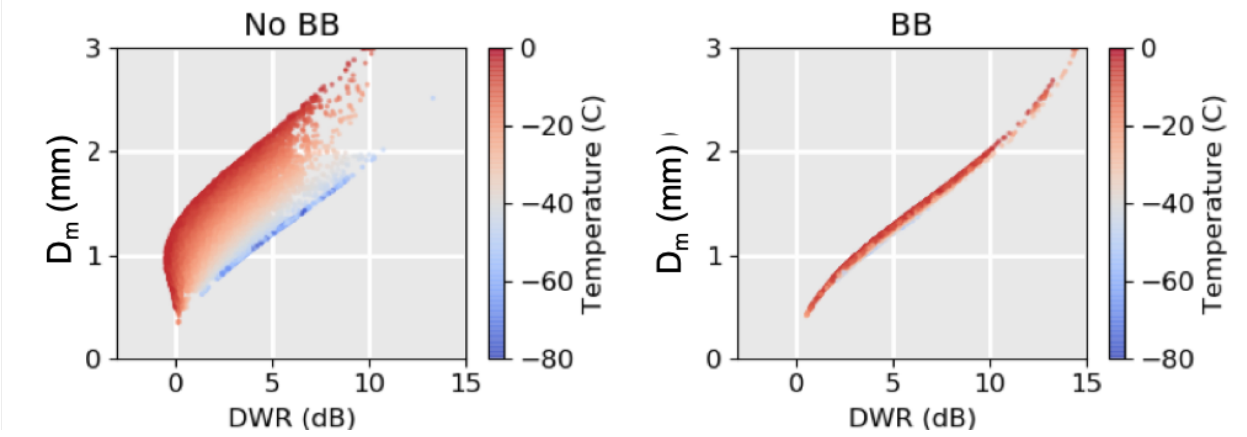

Figure 4.2
2A-DPR simulated DWR-Dm relationships for no BB (left) and BB (right) scenarios implied by collocated DWR and Dm data points.

4.3 RESULTS

4.3.1 EVALUATIONS OF SPHEROID-BASED DWR-D_M RELATIONSHIPS

In Figure 4.3, spheroid DWR-D_m relationships using different parameterizations of AR (AR = 0.3 (Ob), AR = 0.6 (Ob), AR = 0.6 (Pr)) and ODF are evaluated against the combined dataset. Figure 4.3 provides some implications of snow microphysical properties that are otherwise un-measurable in clouds through typical *in-situ* and radar methods. First, while ODF has previously been considered to be an unimportant parameter (Leinonen et al. 2012; Liao et al. 2016), it can have a moderate impact on the simulated DWR of snow particles with very low AR. Such low AR have been suggested as a result of overestimated 2D imagery by Jiang et al. (2017). For exponential size distributions, models based off of randomly aligned snow particles tend to underestimate the measured data to some degree. Simulated relationships that can recreate the empirical relationship, or that can account for measurements that fall above the empirical relationship, require some preferential alignment to approach or exceed the empirical relationship. This provides some evidence that DPR-visible snow PSDs are closer to being horizontally oriented than randomly oriented, a distinction that is still poorly known (Hogan et al. 2012; Jiang et al. 2019). Second, simulated DWR-D_m relationships based off of prolate spheroids are very low-biased, both with respect to the measured data and to the other scattering models considered in this study. This is a surprise, as prolate spheroids are claimed to be a better description of the kind of snowflakes that were measured during GCPEX (Jiang et al. 2019)

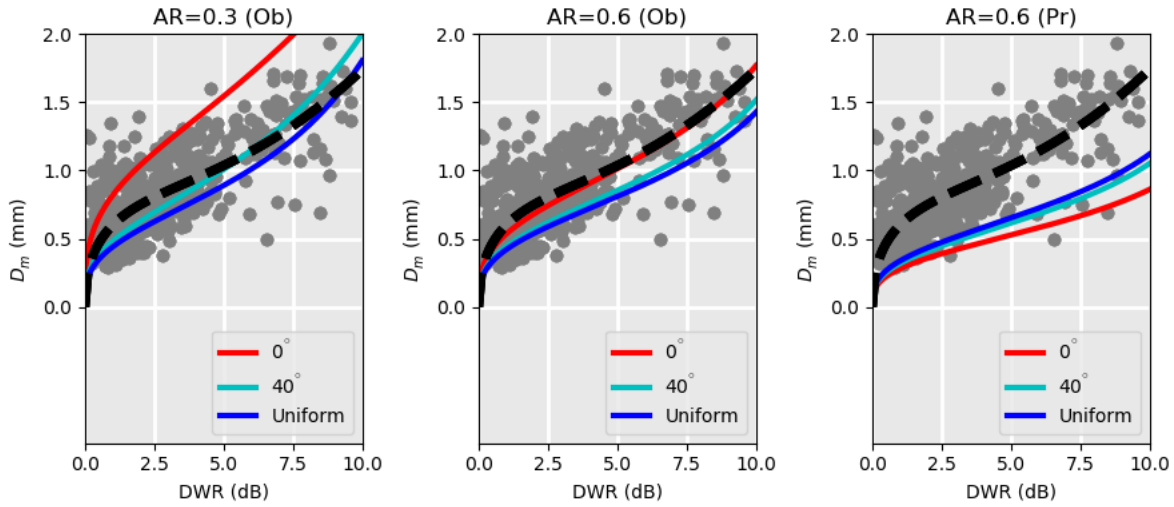

Figure 4.3
Simulated DWR-Dm relationships generated with a variety of microphysical assumptions, compared with the matched data and singular empirical DWR-Dm relationship from Figure 3.7

A near-perfect replication of the empirical relationship can be simulated from a spheroid scattering model under an AR = 0.6 (Ob), μ = 0 parameterization. Remarkably, this parameterization is very similar to the Hogan et al. (2012) recommendation for cloud-ice hydrometeors, just using the Heymsfield et al. (2010) mass parameterization in place of Brown and Francis (1995). This could be an important difference. Changes in *a* and *b* will both change the moment of the measured PSD represented by D_m, but only changes in *b* will impact a spheroid-simulated DWR, and neither will impact the measured DWR used to derive an empirical relationship. Therefore, one may expect that simulated and empirical DWR- D_m relationships will have different sensitivities to changes in mass parameterizations. Simulated and empirical DWR-D_m relationships are generated for spheroids with three different mass parameterization in Figure 4.4. *b* is varied between 1.9, 2.1, and 2.3, and corresponding *a* parameters of 0.003, 0.006, and 0.015 are calculated through the method described in Mason et al., (2018). Other parameters remain fixed with a horizontal orientation, AR = 0.6 (Ob). While the empirical and simulated DWR-Dm relationships both become steeper in response to heavier mass parameterizations, an expected result considering D_m will get larger as *a* and *b* increase, the corresponding increase between the relationships is disproportionate. Lower *b* values lead to an increase in simulated DWR that amplifies the effect of the increased D_m, leading to a

systematically high (low) offset for simulated D_m compared to to the empirical relationship as *b* increases above (decreases below)

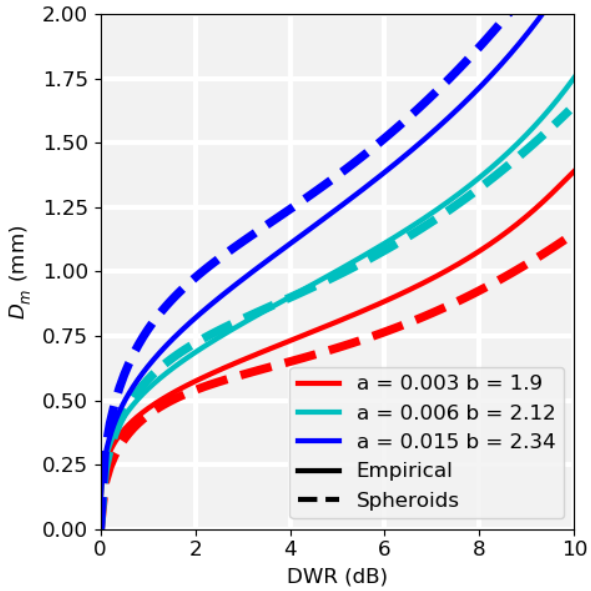

Figure 4.4
Comparison between the empirical relationship and the simulated curve using different mass parameterizations

4.3.2 EVALUATION OF 2A-DPR RETRIEVALS

The assumptions in the 2A-DPR dataset represent the most widely used DWR-based retrievals in the world today, so they adequately represent the real behavior of snow PSDs. In Figure 4.5, 2A-DPR data are evaluated against relevant GV data. GCPEX measurements of snowing clouds above snowstorms are matched to the -5°C < T < -20°C DPR noBB measurements in Figure 4.5a, and MC3E and OLYMPEX measurements of snowing clouds above rainstorms are matched to DPR-BB measurements in Figure 4.5b.

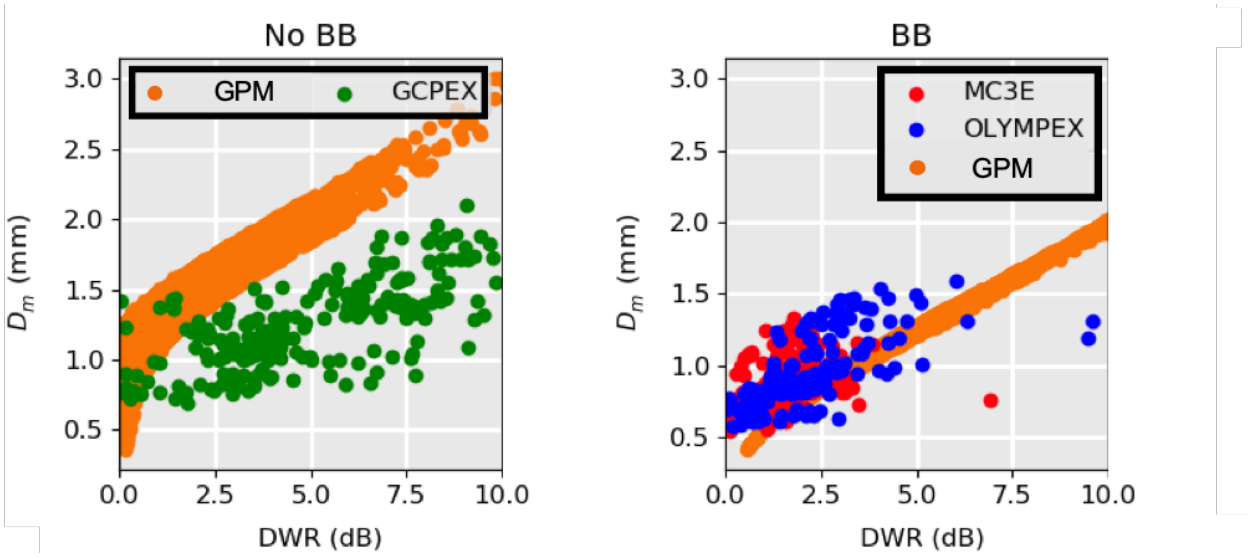

Figure 4.5
Evaluation of 2A-DPR noBB (left) and BB (right) simulated DWR-Dm relationships against comparable experimental data from Chapter 3

Figure 4.5 demonstrates that the 2A-DPR assumptions are biased with respect to the witnessed DWR and D_m in snow clouds. The bias is the largest for the DPR-noBB relationship. This is because the GCPEX DWR-D_m relationship follows the same trajectory as the OLYMPEX and MC3E data, while the temperature-dependent DWR-D_m relationship from the 2A-DPR algorithm differs by a mm between BB and no-BB. The poor recreation of measured DWR-D_m relationships from 2A-DPR assumptions implies a bias for GPM retrievals of snow clouds. To visualize how this bias manifests in real GPM measurements, Figure 4.6 provides the DWR, GPM-retrieved D_m (GPM-D_m), the D_m retrieved through the singular empirical relationship from Chapter 3 (Duffy-D_m), and the difference between the two D_m measurements (ΔD_m) from two selected examples of GPM DWR measurements of storm clouds.

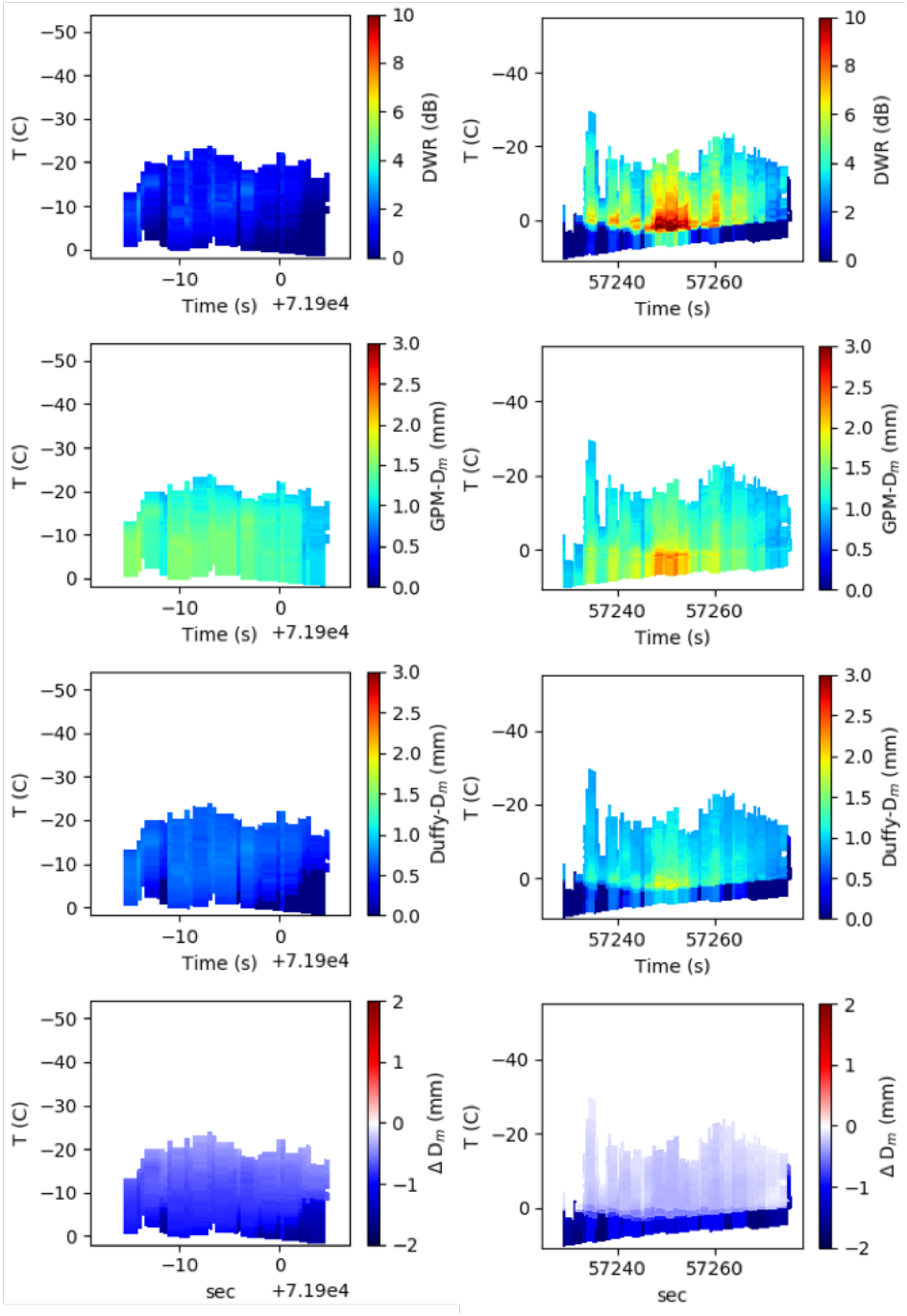

Figure 4.6
Two selected DPR storm overpasses. Top row displays the DPR, second row displays the GESC-retrieved Dm, third row displays the empirically retrieved Dm, bottom row displays the difference between the two Dm measurements.

The left and right column of Figure 4.6 depict storms that were likely formed through similar processes. They both have cloud tops that mostly fall below -20° degrees and surface temperatures a little above 0°C, typical of stratiform precipitating clouds that may generate snow, sleet, or rain depending on the boundary layer temperature profile. The storm in the left column has no bright band and a DWR mostly below 2 DWR, save for a few profiles near 2530 s. The storm in the right column has a DPR-detected bright band, and a DWR approaching 6 dB. Based on the relationship between DWR and D_m predicted from theory (Figure 3.15) and visualized in data (Figure 3.8), the storm with a bright band would therefore be expected to contain a proportionally larger D_m. However, this is only the case for the empirically retrieved D_m, and the difference between the two retrieval algorithms results in the GPM algorithm providing a similar D_m for both storm clouds. As a result, the difference between the Emp-D_m and GESC-D_m for the two storms changes by more than 1.5 mm, despite any apparent evidence that the DWR of the two storms should reflect different cloud properties.

4.4 CONCLUSION

In this chapter, I used experimentally collocated data to evaluate simulated DWR-D_m relationships. I evaluate different realizations of the "spheroid" scattering model and the DWR-D_m relationship used to retrieve precipitation in the DPR-2A algorithm. The results are summarized in the following bullets.

- The empirical relationship is almost near-perfectly represented by a simulated DWR-D_m relationship generated from a spheroid scattering model with an AR of 0.6 (Ob), a 0° delta function (horizontally oriented) ODF, a $\mu = 0$ (exponential) gamma size distribution, an *a* of 0.007 and a *b* of 2.2. This parameterization represents the assumption for cloud ice recommended in Hogan et al. (2012) combined with a mass parameterization for unspecified snow particles from Heymsfield et al. (2010). The agreement between the two relationships fails if other *a* and *b* are considered, however. Therefore, the Hogan et al. (2012) shape and orientation parameterizations can therefore be used to underestimate, overestimate, or accuraretly account for the empirically retrieved D_m depending on the choice of mass

parameterization. This result demonstrates how similarly justifiable assumptions can lead to differing, or even opposing, results when comparing measured and simulated snow PSD properties.

- All prolate-spheroid based relationships substantially underestimate the D_m of the measured data. This result is problematic since prolate spheroids have recently been identified as the best shape to account for the large snow particles that will dominate DPR measurements (Jiang et al. 2019). Therefore, Figure 4.3 implies that a spheroid must be parameterized against the best current knowledge of measured snow particles in order to provide the best agreement to measured data. Considering how pervasive the oblate spheroid approximation is in multiple frequency simulations of snow PSDs (Kneifel et al. 2015; Chase et al. 2018; Leinonen et al. 2012; Liao et al. 2016), this paradox should be a subject of future study.

- The temperature-dependent retrieval assumptions for noBB clouds in the 2A-DPR algorithm implies a very different DWR-D_m relationship for snow clouds above frozen precipitation than for snow clouds above liquid precipitation. This relationship is not witnessed in measured data; rather, snow clouds above rainstorms and snowstorms previously displayed a remarkable level of consistency about a singular empirical relationship. The BB-conditional temperature-dependant DWR-D_m retrieval method in the GPM algorithm leads to visibly unrealistic results in DPR data, where similar clouds will have full mm differences in D_m depending on whether they lie on top of a snowing storm or a rainstorm. In GPM retrievals of storm clouds, the GPM algorithm leads to unexplainably similar measurements of D_m from clouds with very different DWR signatures.

These findings can be summarized into two important problems for satellite retrievals of frozen precipitation. First, the assumptions for frozen precipitation in the GPM algorithm are demonstrably incorrect, both in their basis and in the resulting predictions for precipitation reflectivity. Second, there is not currently a scattering model which is able to adequately recreate measured DWR reflectivity *and* be parameterized according to measured properties of snowflakes. A temperature-independent horizontally aligned spheroid is likely a better choice to base the retrieval model in the 2A-DPR algorithm on than the model currently implemented, at

least for mid-latitude clouds that were represented in Section 2. However, it is problematic that this model requires a knowingly improper assumption for snow axial ratio. High-resolution imagery of the large snowflakes which the DPR specializes in measuring have only become possible within the past few years, and the discovery that the aggregates fall as prolate particles was published just within this past year. Other properties of large snow aggregates may be revealed in coming years which could lead to a DWR-D_m relationship that aligns better with measured values. Further studies on the microphysical properties of large snow aggregates, such as density or orientation, will be valuable to unite my observations of snow particles with predictions from my most naturally representative model

CHAPTER 5 CONCLUSION

Measurements of falling snow represent some of the most poorly understood precipitation on the planet, and only recently have satellite radars been developed which can retrieve snowfall rates over all surfaces and inside of clouds. During my time at Vanderbilt University and the University of Illinois at Urbana-Champaign, I conducted the following research related to satellite radar measurements of snowfall:

- I used *in-situ* and radar measurements of falling snow to develop empirical relationships between DPR measurements and D_m across orographic, convective, and stratiform snowfall in temperatures ranging from 0 to -40°C. Through this research, I demonstrated the superiority of a DWR retireval method, and I generated the first empirical relationship between DWR and D_m that can be recommended for GPM use across the planet.

- I evaluated contemporary scattering models used to represent falling snow in simulations and retrieval algorithms. I demonstrated that there are no current scattering models based on our best available knowledge of snow properties which can recreate the measured relationships between DWR and D_m, and that the current assumptions in the GPM algorithm are particularly unrealistic for stratiform snow clouds. Therefore, the empirical relationship between DWR and D_m from chapter two is encouraged for global retrievals in place of the current 2A-DPR provided values.

- I used CloudSat snowfall measurements in conjunction with climate reanalysis models to determine the impact of melting snow on the ocean surface heat budget, and found it to be influential on instantaneous and seasonal time scales

This dissertation has improved our capabilities to retrieve falling snow information from satellite radars, it has provided new information on the physical tendencies of falling snow, and it has demonstrated new importance of falling snow to planetary processes. Importantly, it also quantifies some of the limitations that the current generation of precipitation radar satellites face in conducting research on global snowfall. The next generation of precipitation radar satellites

are currently in development, and these studies provide essential information on what new capabilities are necessary for future satellites to improve our snow-related knowledge of the planet.

CHAPTER 6 WORKS CITED

Behrangi, A., and Coauthors, 2016: Status of high-latitude precipitation estimates from observations and reanalyses. *J. Geophys. Res. Atmos.*, **121**, 4468–4486, https://doi.org/10.1002/2015JD024546.

Bintanja, R., and O. Andry, 2017: Towards a rain-dominated Arctic. *Nat. Clim. Chang.*, **7**, 263–267, https://doi.org/10.1038/nclimate3240.

Boening, C., M. Lebsock, F. Landerer, and G. Stephens, 2012: Snowfall-driven mass change on the East Antarctic ice sheet. *Geophys. Res. Lett.*, **39**, 1–5, https://doi.org/10.1029/2012GL053316.

Borque, P., K. J. Harnos, S. W. Nesbitt, and G. M. McFarquhar, 2019: Improved parameterization of ice particle size distributions using uncorrelated mass spectrum parameters; results from GCPEx. *J. Appl. Meteorol. Climatol.*, 1657–1676, https://doi.org/10.1175/jamc-d-18-0203.1.

Bromwich, D. H., and Coauthors, 2018: The arctic system reanalysis, version 2. *Bull. Am. Meteorol. Soc.*, **99**, 805–828, https://doi.org/10.1175/BAMS-D-16-0215.1.

Brown, P. R. A., and P. N. Francis, 1995: Improved Measurements of the Ice Water Content in Cirrus Using a Total-Water Probe. *J. Atmos. Ocean. Technol.*, **12**, 410–414, https://doi.org/10.1175/1520-0426(1995)012<0410:imotiw>2.0.co;2.

Chase, R. J., and Coauthors, 2018: Evaluation of Triple-Frequency Radar Retrieval of Snowfall Properties Using Coincident Airborne In Situ Observations During OLYMPEX. *Geophys. Res. Lett.*, **45**, 5752–5760, https://doi.org/10.1029/2018GL077997.

Chaudhuri, A. H., R. M. Ponte, and A. T. Nguyen, 2014: A comparison of atmospheric reanalysis products for the Arctic Ocean and implications for uncertainties in air-sea fluxes. *J. Clim.*, **27**, 5411–5421, https://doi.org/10.1175/JCLI-D-13-00424.1.

Chen, S., and Coauthors, 2016: Comparison of snowfall estimates from the NASA CloudSat Cloud Profiling Radar and NOAA/NSSL Multi-Radar Multi-Sensor System. *J. Hydrol.*, **541**, 862–872, https://doi.org/10.1016/j.jhydrol.2016.07.047.

Christensen, M. W., A. Behrangi, T. S. L'Ecuyer, N. B. Wood, M. D. Lebsock, and G. L. Stephens, 2016: Arctic observation and reanalysis integrated system: A new data product for

validation and climate study. *Bull. Am. Meteorol. Soc.*, **97**, 907–915, https://doi.org/10.1175/BAMS-D-14-00273.1.

Déry, S. J., and R. D. Brown, 2007: Recent Northern Hemisphere snow cover extent trends and implications for the snow-albedo feedback. *Geophys. Res. Lett.*, **34**, 2–7, https://doi.org/10.1029/2007GL031474.

Duffy, G., and R. Bennartz, 2018: The Role of Melting Snow in the Ocean Surface Heat Budget. *Geophys. Res. Lett.*, 9782–9789, https://doi.org/10.1029/2018GL079182.

Field, P. R., and A. J. Heymsfield, 2015: Importance of snow to global precipitation. *Geophys. Res. Lett.*, **42**, 9512–9520, https://doi.org/10.1002/2015GL065497.1.

Grazioli, J., J.-B. Madeleine, H. Gallée, R. M. Forbes, C. Genthon, G. Krinner, and A. Berne, 2017: Katabatic winds diminish precipitation contribution to the Antarctic ice mass balance. *Proc. Natl. Acad. Sci.*, 201707633, https://doi.org/10.1073/pnas.1707633114.

Haynes, J. M., T. S. L'Ecuyer, G. L. Stephens, S. D. Miller, C. Mitrescu, N. B. Wood, and S. Tanelli, 2009: Rainfall retrieval over the ocean with spaceborne W-band radar. *J. Geophys. Res. Atmos.*, **114**, 1–18, https://doi.org/10.1029/2008JD009973.

Henderson, D., T. L'ecuyer, D. Vane, G. Stephens, and D. Reinke, 2011: Level 2B Fluxes and Heating Rates and 2B Fluxes and Heating Rates w / Lidar Process Description and Interface Control Document. *CloudSat Proj. A NASA Earth Syst. Sci. Pathfind. Mission*, 1–28.

Heymsfield, A. J., and J. L. Parrish, 1978: A Computational Technique for Increasing the Effective Sampling Volume of the PMS Two-Dimensional Particle Size Spectrometer. *J. Appl. Meteorol.*, **17**, 1566–1572, https://doi.org/10.1175/1520-0450(1978)017<1566:actfit>2.0.co;2.

——, P. Field, and A. Bansemer, 2008: Exponential Size Distributions for Snow. *J. Atmos. Sci.*, **65**, 4017–4031, https://doi.org/10.1175/2008JAS2583.1.

Heymsfield, A. J., C. Schmitt, A. Bansemer, and C. H. Twohy, 2010: Improved Representation of Ice Particle Masses Based on Observations in Natural Clouds. *J. Atmos. Sci.*, **67**, 3303-3306,3308-3318, https://doi.org/10.1175/2010JAS3507.1.

Hogan, R. J., L. Tian, P. R. A. Brown, C. D. Westbrook, A. J. Heymsfield, and J. D. Eastment, 2012: Radar scattering from ice aggregates using the horizontally aligned oblate spheroid approximation. *J. Appl. Meteorol. Climatol.*, **51**, 655–671, https://doi.org/10.1175/JAMC-D-11-074.1.

Jakobson, E., T. Vihma, T. Palo, L. Jakobson, H. Keernik, and J. Jaagus, 2012: Validation of atmospheric reanalyses over the central Arctic Ocean. *Geophys. Res. Lett.*, **39**, 1–6, https://doi.org/10.1029/2012GL051591.

Jensen, T. G., T. J. Campbell, R. A. Allard, R. J. Small, and T. A. Smith, 2011: Turbulent heat fluxes during an intense cold-air outbreak over the Kuroshio Extension Region: Results from a high-resolution coupled atmosphere-ocean model. *Ocean Dyn.*, **61**, 657–674, https://doi.org/10.1007/s10236-011-0380-0.

Jiang, Z., J. Verlinde, E. E. Clothiaux, K. Aydin, and C. Schmitt, 2019: Shapes and Fall Orientations of Ice Particle Aggregates. *J. Atmos. Sci.*, **76**, 1903–1916, https://doi.org/10.1175/jas-d-18-0251.1.

Kneifel, S., A. von Lerber, J. Tiira, D. Moisseev, P. Kollias, and J. Leinonen, 2015: Observed relations between snowfall microphysics and triple-frequency radar measurements. *J. Geophys. Res. Atmos.*, **120**, 6034–6055, https://doi.org/10.1002/2015JD023156.

Kulie, M. S., and L. Milani, 2018: Seasonal variability of shallow cumuliform snowfall: a CloudSat perspective. *Q. J. R. Meteorol. Soc.*, https://doi.org/10.1002/qj.3222.

Kulie, M. S., L. Milani, N. B. Wood, S. A. Tushaus, R. Bennartz, and T. S. L'Ecuyer, 2016: A Shallow Cumuliform Snowfall Census Using Spaceborne Radar. *J. Hydrometeorol.*, **17**, 1261–1279, https://doi.org/10.1175/JHM-D-15-0123.1.

Leinonen, J., 2014: High-level interface to T-matrix scattering calculations: architecture, capabilities and limitations. *Opt. Express*, **22**, 1655, https://doi.org/10.1364/oe.22.001655.

Leinonen, J., S. Kneifel, D. Moisseev, J. Tyynel??, S. Tanelli, and T. Nousiainen, 2012: Evidence of nonspheroidal behavior in millimeter-wavelength radar observations of snowfall. *J. Geophys. Res. Atmos.*, **117**, 1–10, https://doi.org/10.1029/2012JD017680.

Leinonen, J., and Coauthors, 2018: Retrieval of snowflake microphysical properties from multifrequency radar observations. *Atmos. Meas. Tech.*, **11**, 5471–5488, https://doi.org/10.5194/amt-11-5471-2018.

Li, J.-L. F., and Coauthors, 2016a: Considering the radiative effects of snow on tropical Pacific Ocean radiative heating profiles in contemporary GCMs using A-Train observations. *J. Geophys. Res.*, **121**, 1621–1636, https://doi.org/10.1002/2015JD023587.

Li, L., and Coauthors, 2016b: The NASA High-Altitude Imaging Wind and Rain Airborne Profiler. *IEEE Trans. Geosci. Remote Sens.*, **54**, 298–310, https://doi.org/10.1109/TGRS.2015.2456501.

Liao, L., R. Meneghini, T. Iguchi, and A. Detwiler, 2005: Use of dual-wavelength radar for snow parameter estimates. *J. Atmos. Ocean. Technol.*, **22**, 1494–1506, https://doi.org/10.1175/JTECH1808.1.

——, ——, A. Tokay, and L. F. Bliven, 2016: Retrieval of snow properties for Ku- and Ka-band dual-frequency radar. *J. Appl. Meteorol. Climatol.*, **55**, 1845–1858, https://doi.org/10.1175/JAMC-D-15-0355.1.

Liu, G., 2009: Deriving snow cloud characteristics from CloudSat observations. *J. Geophys. Res. Atmos.*, **114**, 1–13, https://doi.org/10.1029/2007JD009766.

Locatelli, J. D., and P. V. Hobbs, 1974: Fall speeds and masses of solid precipitation particles. *J. Geophys. Res.*, **79**, 2185–2197, https://doi.org/10.1029/jc079i015p02185.

Mason, S. L., C. J. Chiu, R. J. Hogan, D. Moisseev, and S. Kneifel, 2018: Retrievals of Riming and Snow Density From Vertically Pointing Doppler Radars. *J. Geophys. Res. Atmos.*, **123**, 13,807-13,834, https://doi.org/10.1029/2018JD028603.

Matrosov, S. Y., 2007: Modeling Backscatter Properties of Snowfall at Millimeter Wavelengths. *J. Atmos. Sci.*, **64**, 1727–1736, https://doi.org/10.1175/JAS3904.1.

——, and A. J. Heymsfield, 2017: Empirical relations between size parameters of ice hydrometeor populations and radar reflectivity. *J. Appl. Meteorol. Climatol.*, **56**, 2479–2488, https://doi.org/10.1175/JAMC-D-17-0076.1.

Milani, L., and Coauthors, 2018: CloudSat snowfall estimates over Antarctica and the Southern Ocean: An assessment of independent retrieval methodologies and multi-year snowfall analysis. *Atmos. Res.*, **213**, 121–135, https://doi.org/10.1016/j.atmosres.2018.05.015.

Norin, L., A. Devasthale, T. S. L'Ecuyer, N. B. Wood, and M. Smalley, 2015: Intercomparison of snowfall estimates derived from the CloudSat Cloud Profiling Radar and the ground-based weather radar network over Sweden. *Atmos. Meas. Tech.*, **8**, 5009–5021, https://doi.org/10.5194/amt-8-5009-2015.

Palerme, C., J. E. Kay, C. Genthon, T. L'Ecuyer, N. B. Wood, and C. Claud, 2014: How much snow falls on the Antarctic ice sheet? *Cryosphere*, **8**, 1577–1587, https://doi.org/10.5194/tc-8-1577-2014.

Palerme, C., C. Claud, A. Dufour, C. Genthon, N. B. Wood, and T. L'Ecuyer, 2017a: Evaluation of Antarctic snowfall in global meteorological reanalyses. *Atmos. Res.*, **190**, 104–112, https://doi.org/10.1016/j.atmosres.2017.02.015.

——, C. Genthon, C. Claud, J. E. Kay, N. B. Wood, and T. L'Ecuyer, 2017b: Evaluation of current and projected Antarctic precipitation in CMIP5 models. *Clim. Dyn.*, **48**, 225–239, https://doi.org/10.1007/s00382-016-3071-1.

Papritz, L., and T. Spengler, 2017: A Lagrangian climatology of wintertime cold air outbreaks in the Irminger and Nordic Seas and their role in shaping air-sea heat fluxes. *J. Clim.*, **30**, 2717–2737, https://doi.org/10.1175/JCLI-D-16-0605.1.

Partain, P., 2007: Cloudsat ECMWF-AUX auxiliary data process description and interface control document.

Petty, G. W., and W. Huang, 2010: Microwave Backscatter and Extinction by Soft Ice Spheres and Complex Snow Aggregates. *J. Atmos. Sci.*, **67**, 769–787, https://doi.org/10.1175/2009jas3146.1.

Sadowy, G. A., A. C. Berkun, W. Chun, I. W., and S. L. Durden, 2003: Development of an Advanced Airborne Precipitation Radar. *Microw. J.*, **46**, 84–98.

Seto, S., T. Iguchi, and T. Oki, 2013: The Basic Performance of a Precipitation Retrieval Algorithm for the Global Precipitation Measurement Mission's Single/Dual-Frequency Radar Measurements. *IEEE Trans. Geosci. Remote Sens.*, **51**, 5239–5251, https://doi.org/10.1109/TGRS.2012.2231686.

Skofronick-Jackson, G., M. Kulie, L. Milani, S. J. Munchak, N. B. Wood, and V. Levizzani, 2019: Satellite Estimation of Falling Snow: A Global Precipitation Measurement (GPM) Core Observatory Perspective . *J. Appl. Meteorol. Climatol.*, **58**, 1429–1448, https://doi.org/10.1175/jamc-d-18-0124.1.

Smith, S. R., P. J. Hughes, and M. A. Bourassa, 2011: A comparison of nine monthly air-sea flux products. *Int. J. Climatol.*, **31**, 1002–1027, https://doi.org/10.1002/joc.2225.

Sorteberg, A., V. Kattsov, J. E. Walsh, and T. Pavlova, 2007: The Arctic surface energy budget as simulated with the IPCC AR4 AOGCMs. *Clim. Dyn.*, **29**, 131–156, https://doi.org/10.1007/s00382-006-0222-9.

Stephens, G. L. ., and Et.al, 2002: The Cloudsat Mission and the A-Train. *Bull. Am. Meteorol. Soc.*, 1771–1790, https://doi.org/10.1175/BAMS-83-12-1771.

Waliser, D. E., J.-L. F. Li, T. S. L'Ecuyer, and W. T. Chen, 2011: The impact of precipitating ice and snow on the radiation balance in global climate models. *Geophys. Res. Lett.*, **38**, 1–6, https://doi.org/10.1029/2010GL046478.

Wolf, T., I. Esau, and J. Reuder, 2014: Characterizing the radiative impacts of precipitating snow in the ECMWF Integrated Forecast System global model. *J. Geophys. Res. Atmos.*, **119**, 9626–9637, https://doi.org/10.1002/2014JD022085.Received.

Wood, N. B., T. S. L'Ecuyer, D. G. Vane, G. L. Stephens, and P. Partain, 2013: Level 2C snow profile process description and interface control document,. *CloudSat Proj.*,.

Yin, M., G. Liu, R. Honeyager, and F. Joseph Turk, 2017: Observed differences of triple-frequency radar signatures between snowflakes in stratiform and convective clouds. *J. Quant. Spectrosc. Radiat. Transf.*, **193**, 13–20, https://doi.org/10.1016/j.jqsrt.2017.02.017.